

(2)

AD-A240 792

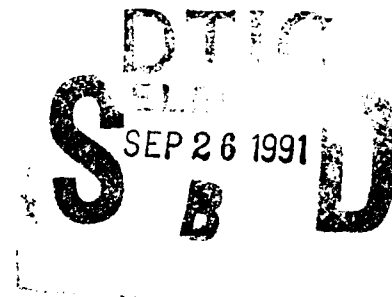
A NOVEL TECHNIQUE TO STIMULATE THE FLOW IN A SOLID PROPELLANT ROCKET

**W.K. Van Moorhem
Yiping Ma
R.W. Shorthill
K. Chen
N. Rao**

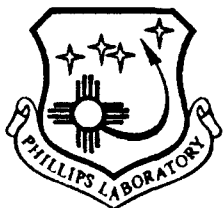
**University of Utah
Mechanical Engineering Dept.
3209 MEB
Salt Lake City, UT 84112**

September 1991

Final Report



APPROVED FOR PUBLIC RELEASE; DISTRIBUTION UNLIMITED.



**PHILLIPS LABORATORY
Propulsion Directorate
AIR FORCE SYSTEMS COMMAND
EDWARDS AIR FORCE BASE CA 93523-5000**

91-11565

9 1 9 25 117


NOTICE

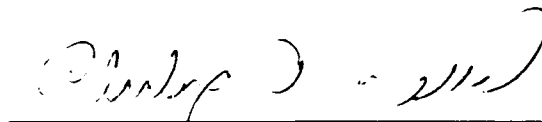
When U.S. Government drawings, specifications, or other data are used for any purpose other than a definitely related Government procurement operation, the fact that the Government may have formulated, furnished, or in any way supplied the said drawings, specifications, or other data, is not to be regarded by implication or otherwise, or in any way licensing the holder or any other person or corporation, or conveying any rights or permission to manufacture, use or sell any patented invention that may be related thereto.

FOREWORD


This final report was submitted by the University of Utah, Salt Lake City UT on completion of contract F04611-86-K-0083 with the OLAC, Phillips Laboratory (AFSC) (formerly Astronautics Laboratory), Edwards AFB CA 93523-5000. OLAC PL Project Manager was Gary Vogt.


This report has been reviewed and is approved for release and distribution in accordance with the distribution statement on the cover and on the SF Form 298.


GARY L. VOGT
Project Manager


PHILIP A. KESSEL
Chief, Thermophysics Branch

FOR THE COMMANDER


DAVID W. LEWIS, MAJOR, USAF
Acting Director
Fundamental Technologies Division


RANNEY G. ADAMS
Public Affairs Director

REPORT DOCUMENTATION PAGE			Form Approved OMB No. 0704-0188	
<small>Public reporting burden for this collection of information is estimated to average 1 hour per response, including the time for reviewing instructions, searching existing data sources, gathering and maintaining the data needed, and completing and reviewing the collection of information. Send comments regarding this burden estimate or any other aspect of this collection of information, including suggestions for reducing this burden, to Washington Headquarters Services, Directorate for Information Operations and Reports, 1215 Jefferson Davis Highway, Suite 1204, Arlington, VA 22202-4302, and to the Office of Management and Budget, Paperwork Reduction Project (0704-0188), Washington, DC 20503.</small>				
1. AGENCY USE ONLY (Leave blank)		2. REPORT DATE Sept 91	3. REPORT TYPE AND DATES COVERED Final 8/86 to 6/90	
4. TITLE AND SUBTITLE A Novel Technique To Simulate The Flow In A Solid Propellant Rocket			5. FUNDING NUMBERS PE: 62302F PR: 5730 TA: 00PY G: F04611-86-K-0083	
6. AUTHOR(S) W.K. Van Moorhem, Yiping Ma, R.W. Shorthill, K. Chen, N. Rao				
7. PERFORMING ORGANIZATION NAME(S) AND ADDRESS(ES) University of Utah Mechanical Engineering Dept. 3209 MEB Salt Lake City, UT 84112			8. PERFORMING ORGANIZATION REPORT NUMBER	
9. SPONSORING/MONITORING AGENCY NAME(S) AND ADDRESS(ES) OLAC/Phillips Laboratory PL/RFT Edwards AFB, CA 93523-5000			10. SPONSORING/MONITORING AGENCY REPORT NUMBER AL-TR-90-080	
11. SUPPLEMENTARY NOTES COSATI Codes: 21/02; 21/09				
12a. DISTRIBUTION/AVAILABILITY STATEMENT Approved for Public Release Distribution is Unlimited			12b. DISTRIBUTION CODE	
13. ABSTRACT (Maximum 200 words) An experimental study has been carried out to investigate the occurrence of acoustically generated turbulence and the possible role of this turbulence in the velocity coupling phenomenon that is believed to occur in some acoustically unstable solid propellant rocket motors. A new technique has been developed to carry out this investigation. The burning propellant is simulated by subliming dry ice. This simulation allows relatively long run times and ease of instrumentation as compared to using actual propellants. The technique also reduces the possibility of turbulence being generated by the injection process in a "cold flow" simulation. Subliming dry ice also has a positive pressure exponent, similar to, but weaker than, an actual propellant. In the experiment a small section of dry ice is contained in a closed tube approximately two meters long which is equipped with a mechanically driven piston at one end. This piston is used to produce strong pressure and velocity waves which propagate over the dry ice.				
-continued-				
14. SUBJECT TERMS velocity coupling, dry ice simulation, acoustically induced transition to turbulence, pressure coupling, solid rocket motor stability, "cold flow" simulation			15. NUMBER OF PAGES 78	
			16. PRICE CODE	
17. SECURITY CLASSIFICATION OF REPORT Unclassified	18. SECURITY CLASSIFICATION OF THIS PAGE Unclassified	19. SECURITY CLASSIFICATION OF ABSTRACT Unclassified	20. LIMITATION OF ABSTRACT SAR	

Three primary methods have been used to investigate the flow field: flow visualization, making use of the water vapor fog layer that occurs near the dry ice surface; hot film measurements; and mass flow measurements. Laser Doppler anemometry was also attempted but failed to produce meaningful results. Measurements of the amplitude and time history of the pressure waves in the chamber were also made. The experiments were generally carried out by varying the frequency of the piston oscillations from zero to a speed near the natural frequency of the first longitudinal acoustic mode of the chamber. Since the piston motion was not purely sinusoidal, harmonics of the piston frequency could drive weak resonances in the tube. Such resonances were routinely observed with the piston operating at one-half and one-third of the first acoustic mode of the gas in the tube. These resonances were caused by the first and second harmonics of the piston motion. Making use of this characteristic of the experiment allowed different amplitude and frequency waves to be investigated.

Flow visualization clearly demonstrated that turbulent flow occurred above the dry ice with sufficiently strong waves. The experiment was carried out with the dry ice located both at the head end and near the center of the chamber. With the dry ice near the center of the chamber, the amplitude of the waves, expressed in terms of a local acoustic Reynolds number, was in the range found by previous investigators to produce transition where side wall injection was not present. The transition acoustic Reynolds number was about a factor of two lower than that predicted by a numerical model that considered isothermal flow over a smooth surface with no initial turbulence. When the dry ice was located at the head end of the chamber, the transition occurred at a local acoustic Reynolds number which was an order of magnitude lower than that observed previously. This dependence on position, is believed to be due to acoustic streaming effects, which were observed in the flow visualization. The acoustic velocity distribution in the first longitudinal mode would require transition to occur initially at the center of the tube, where the largest velocity oscillations occur. Acoustic streaming produces a steady flow, near the tube walls, from the center of the tube toward the ends. This steady flow is believed to convect the locally generated turbulence from the center of the tube toward the ends producing the premature transition observed at the head end.

Hot film anemometry produced results in general agreement with the observations from flow visualization. Quantitative velocity measurements with the hot film technique were prevented by the very strong temperature gradients near the dry ice. In addition, there is no accepted definition for the determination of the initiation of turbulent flow from hot film data. This is further complicated by the unsteady character of this flow.

Measurements of the mean mass flow rate of the gas leaving the chamber showed that the mass flow was nearly constant when the flow over the dry ice was believed to be laminar. Following transition to turbulence the mass flow rate increases. The percentage increase in the mass flow rate, beyond the laminar value, was found to be proportional to the fractional increase in the acoustic Reynolds number, beyond the transition value, to the 0.8 power ($Re_a^{0.8}$). This same behavior is found in the available data for experiments using actual rocket propellant where velocity coupling was believed to be present.

Measurements of the amplitude of the oscillating pressure in the tube showed a major peak at the tube resonant frequency, as expected, and minor peaks at the piston frequencies corresponding to one-half and one-third the resonant frequency. The data also showed a weak, but clear and repeatable, dependence on whether or not the tube contained dry ice, the rate of sublimation of the dry ice and the location of the dry ice in the tube. The largest amplitudes were observed with dry ice located near the center of the tube and subliming at the highest achievable rate. The center of the tube is an oscillating velocity antinode when the tube is driven at the first resonant frequency. As the sublimation rate was decreased, the amplitude decreased to the value obtained with the dry

-continued-

ice absent and replaced with an aluminum plate. Smaller amplitude oscillations were obtained when the dry ice section was moved to the head end of the chamber. Replacing the dry ice with an aluminum plate gave the largest amplitude oscillations at the head end, but the amplitude was smaller than those achieved at the center. The cases with dry ice, at the head end, produced yet smaller amplitude oscillations. The sublimation rate appeared to have little effect on the amplitude at the the head end location. A number of explanations for these effects have been considered. The most likely is that with the dry ice near the center a velocity coupling effect is present. When the dry ice is at the head end of the chamber, velocity coupling does not occur, but rather the finite acoustical impedance of the porous dry ice dominates.

This experiment has successfully investigated the acoustically generated transition to turbulence and has produced a velocity coupling-like effect on the amplitude of the oscillations. Since the increase in mass flow from the dry ice can only be caused by an increased heat transfer to the dry ice under turbulent conditions, this turbulent heat transfer must be proportional to $Re_g^{0.8}$. These findings form a base for future modelling of the actual velocity coupling phenomenon in stable solid propellant rocket motors.



Accession For	
NTIS GRA&I	<input checked="" type="checkbox"/>
DTIC TAB	<input type="checkbox"/>
Unannounced	<input type="checkbox"/>
Justification	
By	
Distribution/	
Availability Codes	
Dist	Avail and/or Special
A-1	

TABLE OF CONTENTS

INTRODUCTION	1
EXPERIMENTAL APPROACH	5
Basic Concept	5
Dry Ice Characteristics	6
Chamber Characteristics	9
Flow Measurements	12
Mass Flow Measurements	12
Pressure Measurements	12
Hot Film Anemometry	12
Laser Doppler Anemometry	13
RESULTS	14
Steady Flow Rates	14
Acoustic Characteristics	15
Acoustically Generated Turbulence	22
Transition to Turbulence	22
Flow Visualization Results	22
Hot Film Results	28
Mass Flow and Heat Transfer Results	42
Transition Reynolds Numbers	51
Laser Doppler Flow Field Measurements	53
Laser Doppler Anemometry Results	53
Particle Dynamics	54
CONCLUSIONS	65
REFERENCES	67

INTRODUCTION

Solid propellant rocket motors frequently exhibit combustion instability during their operation. Combustion instability can appear in several forms. A common type is due to pressure oscillations at a frequency corresponding to the fundamental acoustic mode of the motor. Lower frequency oscillations correspond to a longitudinal acoustic mode while higher frequency oscillations result from transverse oscillations. In order for an instability to occur, energy must be fed into the acoustic field at a rate exceeding the loss of energy from the acoustic mode. This results in a growing amplitude of the oscillation, an instability of that acoustic mode.

This concept was first formalized in a realistic mathematical model by Hart and McClure [1] and refined by Culick [2-4]. Although there are a number of sources and sinks of acoustic energy in motors, the major gain is due to the dynamic response of the combustion process to the acoustic oscillations. A solid propellant motor has the potential to be a self excited oscillator, a system that can spontaneously begin to oscillate without any external driving.

The combustion response to acoustic oscillations is a complicated nonlinear phenomenon dependent on the fluid mechanics, heat and mass transfer and chemistry occurring in the gas phase and the heat transfer and chemistry that occur in the solid phase (and possible liquid phase) of the propellant. Of course, simplified models have been developed for this complicated behavior. The most accepted of these models is the concept of pressure coupling of the combustion. In this model the amplitude of the oscillating mass flow from the burning surface is assumed to be proportional to the amplitude of the oscillating pressure in the acoustic field. The constant of proportionality is a complex quantity permitting a phase shift between the mass flow and pressure oscillation. This model has been extensively investigated both analytically and experimentally and is widely accepted as a simple, but realistic, model of the dynamic combustion process.

A more controversial model of combustion assumes that the burning rate is dependent on the amplitude of the velocity parallel to the burning surface, an effect called velocity coupling. Although earlier experimental evidence of this effect exists [5], the experimental results of Crump and Price [6] kindled interest in the effect. Crump and Price burned propellant in a small experimental apparatus with an unstable first longitudinal mode. Before the propellant was totally consumed they quenched the combustion and then observed the contour of the burning surface of the remaining propellant. Their results are shown in Figure 1. It is clear from this data that the burning rate is higher in the center of the propellant grain, a point where the amplitude of the velocity is highest, a velocity antinode, and the burn rate appears to be proportional to the amplitude of the velocity oscillations along the length of the propellant grain.

Following the work of Crump and Price a number of investigators [7-10] considered aspects of the phenomenon but failed to give any insight into the basic mechanism of velocity coupling. Medvedev and Revyagin [11] reporting an experiment very similar to Crump and Price state that "the increase in the combustion

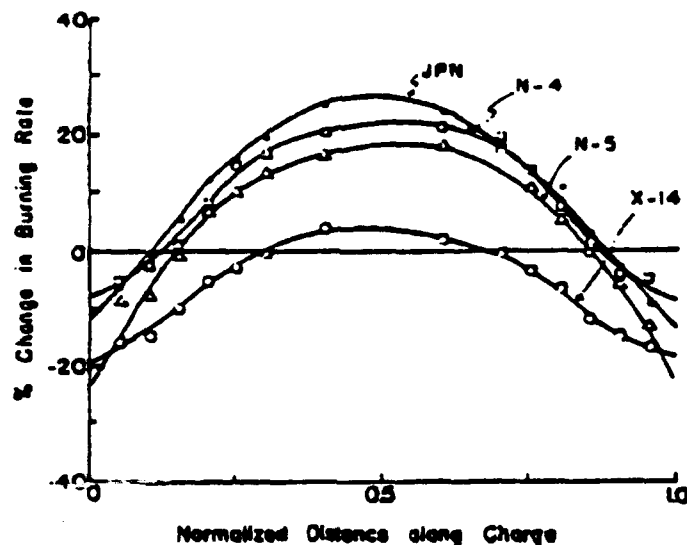


Figure 1
Change in the burning rate as a function of position for several
propellants, from [6]

rate at an antinode of the velocity of the acoustical wave probably occurs as a result of a rise in the coefficient of thermal conductivity of the gaseous medium with its turbulization by acoustic waves." Beddini and Roberts, in a series of papers [12- 14], investigated the occurrence of acoustically generated turbulence by numerical simulation. They included the effect of wall injection simulating the burning of a propellant. Their results, for an isothermal flow with no initial turbulence and a perfectly smooth wall, indicate that low injection velocities initially decrease the acoustic amplitude needed for transition from the no injection case. As the injection velocity increases the acoustic amplitude required for transition passes through a minimum and increases to a value similar to the no-injection case. If there is initial turbulence the minimum may not exist and the required acoustic amplitude may continue to decrease from the no injection case.

Beddini and Roberts collapsed their results into a single transition curve by plotting them in terms of an acoustic Reynolds number, a Reynolds number where the velocity is the amplitude of the acoustic velocity oscillations and the length scale is the thickness of the Stokes layer [15] and an injection Reynolds number based on the injection velocity and the Stokes layer thickness. An acoustic boundary layer or Stokes layer occurs in an oscillatory flow over a solid boundary due to the no-slip condition at the wall. The instability of the Stokes layer has been investigated by several researchers [16-24]. Previous experiments have been limited to the study of the transitional behaviors of the Stokes layer over a nontranspiring smooth surface. Under this condition, the thickness of the Stokes layer, δ , is given as $(2\nu / \omega)^{1/2}$, where ν and ω are the kinetic viscosity and angular frequency of oscillation respectively.

Early investigators discovered that the transition of the Stokes layer into turbulence is governed by the Reynolds number based on the thickness of the Stokes layer $Re_\delta = U\delta/\nu$ or as used in this study $Re_a = \pi^{1/2} Re_\delta = U/(f\nu)^{1/2}$, where U is the amplitude of oscillatory velocity and f is the frequency of the oscillation. The critical Reynolds numbers (Re_a) for transition to occur have been reported as 194.7 [9], 283 [17], 885 [18] and 1000 [19] in these investigations. It was assumed that turbulence occurred over the entire cycle of oscillation.

The work of Merkli and Thomann [20] conducted in piston driven resonant pipe revealed that the turbulence occurred only near the peaks of velocity oscillation. The flow recovered to laminar conditions during the remainder of the cycle. They observed a critical Reynolds number, Re_a , of 500. This value was obtained through hot film anemometry and flow visualization. The onset of any instability in the flow pattern observed in flow visualization was taken to be the onset of turbulence.

The most comprehensive study of the situation was reported by Hino and coworkers [21 - 22]. They have classified the flows into four categories: 1) laminar; 2) weakly turbulent, as indicated by low amplitude high frequency disturbance that appeared during the acceleration phase; 3) conditionally turbulent, which is characterized by a bursting type of turbulence appearing at the start of deceleration phase with the recovery of laminar flow at a later stage during the deceleration phase or early stage of acceleration phase; and 4) fully turbulent flow over whole cycle of oscillation. They further argued that the weakly turbulent flow is triggered by shear instability while the conditional turbulent flow is bursting-like as indicated by ejection of eddies outwards from the boundary. The flow in the last category has not been observed to occur in their experiments or any other experiments reported afterwards. A new Stokes parameter $I = d/(2\delta)$ was introduced by Hino, et al. as a measure of the ratio of a physical dimension of the experiment to the Stokes layer thickness, where d is the characteristic dimension of the apparatus, such as diameter of a pipe or width of a channel. It was found by Hino and his coworkers that the conditional turbulent flow (category 3) occurred at a critical Reynolds number (Re_a) of 974 independent of the value of I . This value was later confirmed by Ohmi, et al. [23] and Akhavan-Alizadeh [24]. The weakly turbulent flow (category 2) has been observed to occur by Hino, et al. at a Reynolds number, Re_a , of 320 to 670 dependent on the value of I . The work of Ohmi and his coworkers, however, have shown that this type of flow occurs at a Reynolds number Re_a of 500 independent of I . This value coincides with the result of Merkli and Thomann, where no differentiation between flow categories 2 and 3 was made. It appears to the authors that the onset of turbulence based on the flow visualizations reported by Merkli and Thomann would be an indication of turbulence in category 2.

It should be pointed out again that, to the authors' knowledge, no previous experiments have been conducted to study the transitional behavior of an oscillatory flow over a transpiring surface, such as in a solid propellant rocket motor. Moreover, none of the existing experiments considered the transition near a velocity node, since it was assumed that the Reynolds number was the dominant factor in determining transition. The rocket situation is further complicated since the process of surface mass addition is coupled with the flow oscillation.

Current experimental approaches in the study of instability in solid propellant rocket motors can be generally divided into two groups, those using actual rocket propellant and "cold flow," room temperature, experiments. Experiments using real rocket propellant result in a very high temperature and pressure environment making measurements very difficult. In the case of a "cold flow facility" where the combustion process is simulated by injecting room temperature gas through a porous surface, a serious disadvantage is that the injection process itself may cause turbulence. The disadvantages of currently available experimental approaches suggested that a new method of investigation was needed to study the combustion instability problem, particularly as related to turbulence.

The primary focus of this research is the velocity coupling phenomenon. The major questions to be answered through this study are: 1) Is it possible for turbulence to occur in the presence of side wall mass injection and when does the transition occur; 2) Does a velocity coupling phenomenon exist in a rocket or in the experiment and 3) What is the role played by turbulence in velocity coupling?

The second section of this report discusses the experiment, how it was designed and operated. The third section describes the results obtained from the experiment. Finally in the last section the conclusions obtained from these results are discussed in terms of their implication to velocity coupling.

EXPERIMENTAL APPROACH

Basic Concepts

Previous experimental work has made use of two approaches: the use of actual rocket propellants or room temperature (cold flow) gas injection simulations. Both of these methods have advantages and disadvantages but neither is well suited to an investigation of acoustically induced turbulence. The use of actual propellant, of course, has the advantage of being an exact simulation. Burning propellant is difficult to instrument and produces very short duration experiments with the amounts normally used in laboratory experiments. Cold flow experiments are relatively easy to instrument and can be run for relatively long durations, but raise questions concerning: 1) the generation of turbulence during the flow injection process; 2) the response of the flow injection process to pressure oscillations and 3) the loss of acoustic energy from the chamber through the pores where the flow is injected.

The present experiment makes use of a new approach using subliming dry ice to simulate burning propellant, Figure 2. The gas generated by the sublimation forms the flow to be investigated. The dry ice is exposed to infrared radiation to increase the sublimation rate. On one end of the chamber, Figure 3, a piston is used to excite acoustic waves in the chamber. These waves then pass over the subliming dry ice; it is the interaction of these waves with the flow generated by the sublimation that is of interest in this project. At the end of the chamber, near the piston, is an exit orifice where the flow exits the chamber.

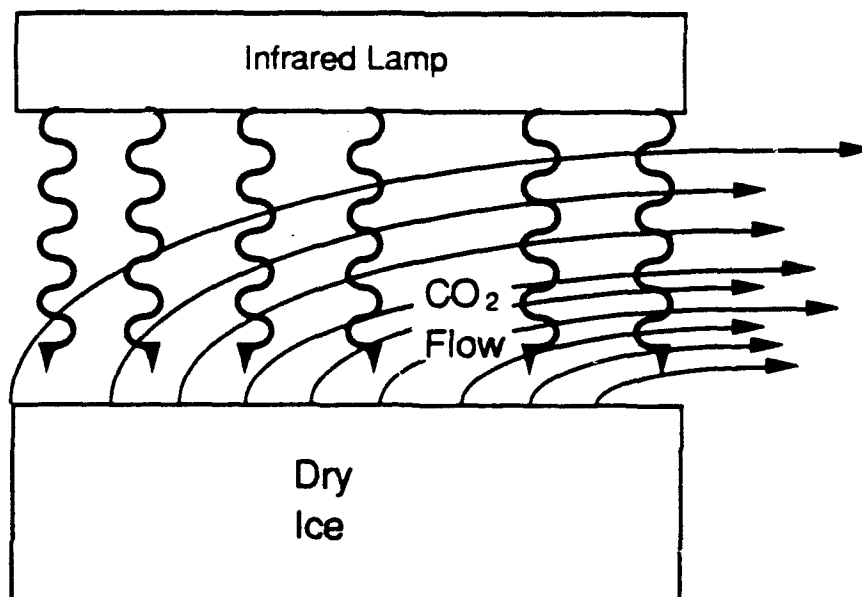


Figure 2

The basic concept of the simulation is to use the gas generated by the enhanced sublimation of dry ice to represent the flow generated by a burning propellant

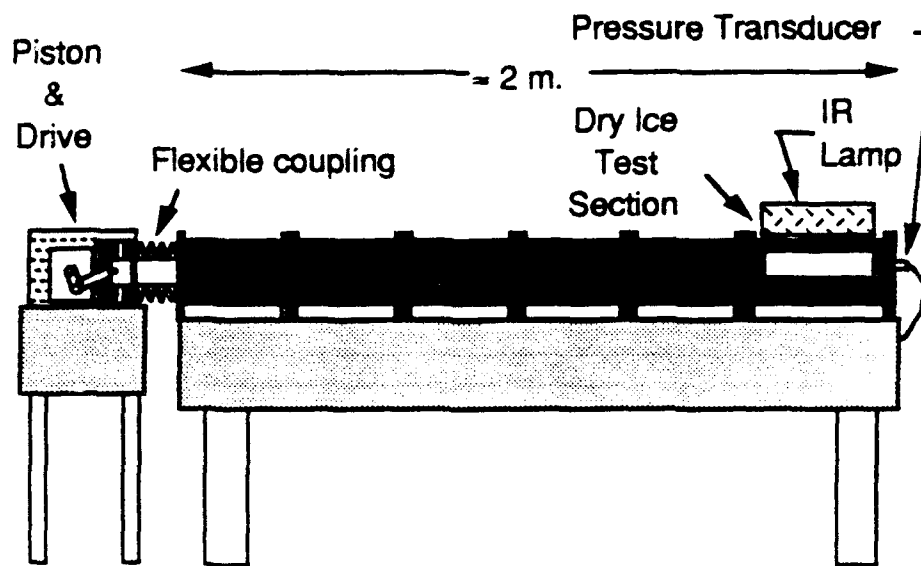


Figure 3

The subliming dry ice is contained in a tube about 2 m. long and constructed from six modular sections, at one end of the tube is a piston which is used to generate waves in the tube and an outlet for the gas generated by the sublimation

Dry Ice Characteristics

Most of the dry ice used in the experiments was commercial dry ice. Commercial dry ice is produced by "snowing" dry ice crystals obtained by throttling liquid carbon dioxide to atmospheric pressure and then compressing the "snow" into a block. A small amount of water, about 1% by weight, is normally added to act as a binder for the compacted dry ice. Pump oil is also present in the dry ice in small quantities. Dry ice can also be prepared in a continuous crystalline form by cooling liquid carbon dioxide at constant pressure. This process produces a material more analogous to an ice cube than the more common compressed dry ice "snow." Most available data on dry ice is for the continuous crystalline form.

Table 1 gives some thermodynamic information on the transition from the solid to gaseous state. Similar information is available in graphical form [25]. Based on these properties, if heat can be added to dry ice at a rate 4.8 kW, the sublimation rate should be 0.00837 kg/sec. (or a volume flow rate of 0.00305 m³/sec). If this mass flow left a dry ice surface of 7.62 by 22.68 cm (as used in this experiment) uniformly at the density and temperature of saturated vapor, the average flow velocity at the surface would be 0.177 m/sec. and the Mach number 0.00081. This represents a surface regression rate of .31 mm/sec. These figures, of course, would represent the maximum possible injection and regression rates for a 4.8 kW heat input. In an actual situation a significant fraction of the radiation from the infrared source will be lost and not all of the radiation reaching the surface of the dry ice will be absorbed, so the actual injection and regression rates will be much lower than the values presented

Table 1: Thermodynamics properties of the solid - vapor transition of carbon dioxide [25]

Temp. °C	Press. Atm.	Density		Specific Enthalpy		Heat of Vaporization kJ/kg	Specific Entropy	
		Solid kg/m ³	Vapor kg/m ³	Solid kJ/kg	Vapor kJ/kg		Solid kJ/kgK	Vapor kJ/kgK
-100.	0.142	1590.	0.428	45.636	630.95	583.32	2.5104	5.8908
-95.	0.236	1590.	0.694	51.079	633.88	582.80	2.5431	5.8150
-90.	0.379	1582.	1.03	56.940	637.23	580.29	2.5749	5.7435
-85.	0.596	1574.	1.67	62.802	640.16	577.36	2.6059	5.6748
-80.	0.914	1566.	2.51	68.664	642.67	574.01	2.6373	5.6095
-78.9	1.00	1566.	2.74	70.045	643.18	573.13	2.6435	5.5948
-75.	1.37	1556.	3.72	74.944	645.19	570.24	2.6695	5.5467
-70.	2.02	1546.	5.39	82.061	646.86	564.80	2.7043	5.4860
-65.	2.93	1534.	7.73	90.016	648.54	558.52	2.7428	5.4261
-60.	4.18	1522.	11.0	99.227	649.37	550.15	2.7863	5.3671
-56.6	5.28	1513.	13.9	105.51	649.37	543.87	2.8156	5.3273

above. The main absorption bands for carbon dioxide are at 2.7, 4.3 and 11.4 to 20 μ m [26]. Weaker absorption bands are at 1.4, 2.0, 4.8, 5.2, 9.4 and 10.4 μ m. If the radiation from the infrared source was concentrated in a narrow band of wavelengths surrounding a major absorption band, a large fraction of the radiation reaching the dry ice would be absorbed. If the source had a narrow bandwidth but was not at an absorption peak, or if the source emitted the radiation over a broad range of wavelengths, the fraction of the infrared radiation reaching the surface and absorbed would be much lower.

A simple model representing the behavior of the dry ice in an unsteady flow field can be obtained by noting that the heat of sublimation of dry ice decreases with increasing pressure, Figure 4, (this is characteristic of all materials). For small changes in pressure this can be approximated by

$$\Delta H_{sub} = \Delta H_o + \left[\frac{d \Delta H}{d P} \right] (P - P_o) \quad (1)$$

where P_o is the initial pressure and ΔH_o the corresponding enthalpy of sublimation and P and ΔH_{sub} the pressure and enthalpy of sublimation at a pressure slightly different than the initial value. Dividing the enthalpy of sublimation, ΔH_{sub} , into a constant heat input rate, Q , yields the mass flow rate from the surface

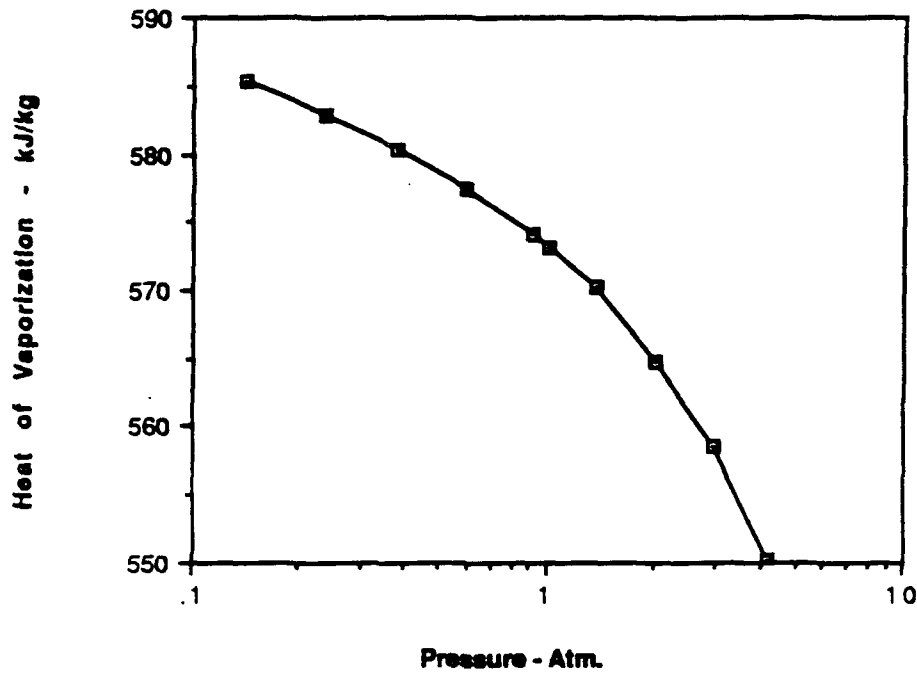


Figure 4.
Heat of vaporization of solid carbon dioxide as a function of pressure

$$m_o + m' = \frac{Q}{\Delta H_o + \left[\frac{d\Delta H}{dP} \right] (P - P_o) + \dots} \quad (2)$$

which is slightly different from the value that would occur at a pressure P_o of m_o . This result can be approximated as

$$\dot{m}_o + \dot{m}' = \frac{\dot{Q}}{\Delta H_o} \left[1 - \frac{1}{\Delta H_o} \left[\frac{d\Delta H}{dP} \right]_o (P - P_o) + \dots \right] \quad (3)$$

and

$$\frac{\dot{m}'}{\dot{m}_o} = - \frac{1}{\Delta H_o} \left[\frac{d\Delta H}{dP} \right]_o (P - P_o) \quad (4)$$

A very similar form can be obtained if

$$\dot{m} = K P^n \quad (5)$$

as is frequently assumed for a burning propellant. If the pressure is changed from P_o , where the mass flow is \dot{m}_o , to P , the mass flow then can be approximated as

$$\dot{m}_o + \dot{m}' = K P_o^n \left[1 + n \frac{P - P_o}{P_o} + \dots \right] \quad (6)$$

or

$$\frac{\dot{m}'}{\dot{m}_o} = n \frac{P - P_o}{P_o} + \dots \quad (7)$$

Comparing equations (4) and (7) it is clear that for small pressure changes the dry ice behaves like a propellant with a pressure exponent of

$$n = - \frac{P_o}{\Delta H_o} \left[\frac{d \Delta H}{d P} \right]_o \quad (8)$$

For a P_o of one standard atmosphere this works out to $n = 0.017$, an extremely weak pressure dependence but at least possessing the same sign as that of a real propellant.

Chamber Characteristics

Figure 5 shows a photograph of the actual chamber. The main structure consists of six interchangeable modules. Five of these modules are approximately 30 cm (12 in) long with a 7.62 cm (3 in) square opening which forms the chamber through which the carbon dioxide gas flows. These five sections are constructed from aluminum, although a plexiglas section of similar dimensions is available.

The sixth section, which contains the dry ice also has a 7.62 cm square cross section. This section is about 43 cm (17 in) long. If the dry ice section is contained between two of the simple tubular modules then the full length of 43 cm is used. When the dry ice section is located near the head end of the chamber an end window allowing a view along the long axis of the chamber reduces the length to approximately 32 cm (12.5 in). Figure 6 shows a cross section of the dry ice module with the end window in place. When the dry ice is in position it covers the full width of the bottom of the chamber for a length of approximately 28 cm (8 in) extending to the end window, when the window is used, or to a distance of 11 cm (4.5 in) from the upstream junction with the next module when the window is not used. Three windows

are located on the sides and top of the dry ice section. The top window is 7.62 cm by 22.86 cm (3 by 9 in) and contains quartz glass to efficiently transmit the infrared radiation from the lamp. The side windows normally contain optical quality windows for visually observing the flow from the dry ice. One or both of these side windows can be replaced with aluminum plates to allow transducers to be mounted above the dry ice.

A coupling to reduce the transmission of vibrations is located between the piston and the chamber. This coupling is 16.7 cm (10.5 in) long. The total length of the

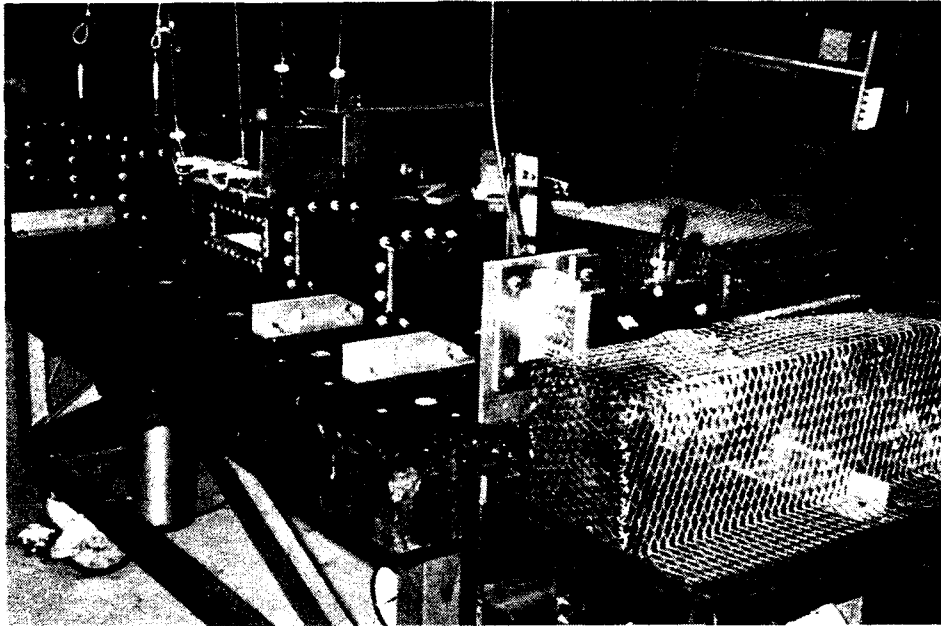


Figure 5
Photograph of the actual experimental chamber

interior of the chamber (measured to the piston at its maximum extension) with the dry ice at the head end is 213. cm (84 in) or with the dry ice at a location other than the head end is 225. cm (88.5 in). The piston and its drive system are located on a separate table from the main chamber to decrease vibration in the chamber. The chamber itself is located on a massive optical table.

Two infrared sources were used to increase the sublimation rate of the dry ice. Both sources had a maximum electrical input of 4.8 kW and an output approximating a black body distribution with the peak at 1.2μ at full power. The source used during most of the work uses four lamps and a reflector consisting of a white insulating material. This unit and the power controller manufactured by Argus International. The second source made use of the same lamps and controller but was constructed with an air cooled, gold plated reflector. The gold plated reflector appeared to supply about 30% more heat to the dry ice than the commercial unit. The need to keep the gold plating extremely clean restricted its usage.

The piston used to generate the waves in the chamber was adapted from a small two cycle engine. The intake and exhaust ports associated with the cylinder in which the piston oscillates have been sealed and the cylinder head removed. The piston is driven through the engine crankshaft and connecting rod by a variable speed electric motor with a feedback speed control system. The connection between the electric motor and the engine crankshaft is via pulleys and a toothed belt to prevent any slippage. Using a crankshaft - connecting rod driven piston is an extremely convenient method, but it has the disadvantage that the piston motion is not a pure sinusoidal motion.

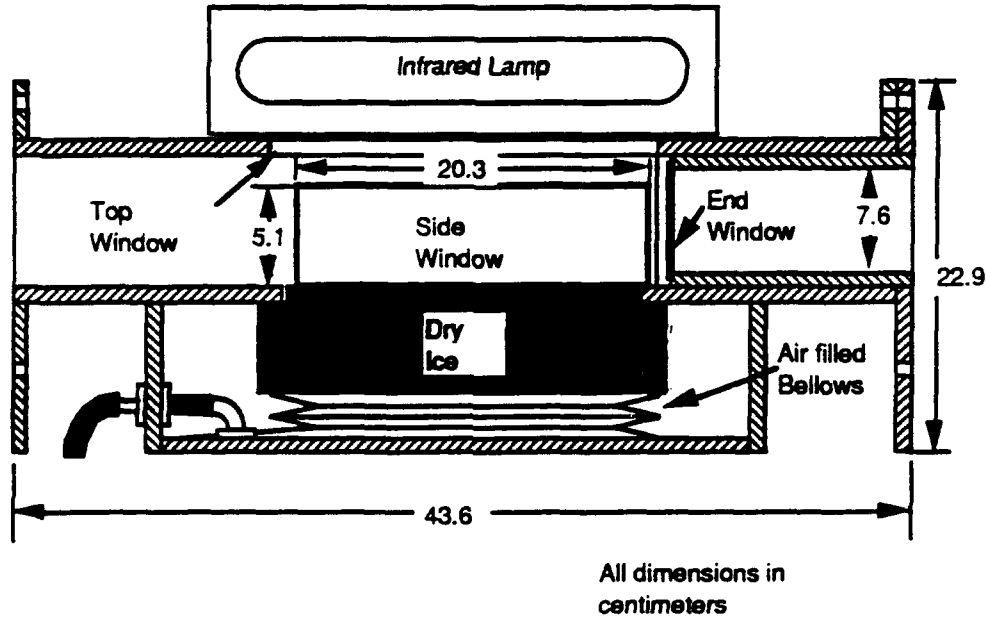


Figure 6.

The dry ice is held in place by the chamber floor and a pressurized air bellows beneath it

The piston position, x , for a piston, connecting rod and crankshaft system is given by the expression

$$x = r \cos \omega t + l \sqrt{1 - \left(\frac{r}{l}\right)^2 \sin^2 \omega t} \quad (9)$$

where r is the offset of the crankshaft throw and l is the length of the connecting rod. For the engine used $r = 19.1 \text{ mm}$ (0.75 in.) and $l = 69.9 \text{ mm}$ (2.75 in.). If this motion is expressed in the form of a Fourier series, with the assumption of small values of r/l , the series would be of the form

$$x = l \left(1 - \frac{1}{4} \left(\frac{r}{l}\right)^2 - \frac{3}{64} \left(\frac{r}{l}\right)^4 + \dots \right)$$

$$\begin{aligned}
& + r \cos \omega t \\
& + \left[\frac{1}{4} \left(\frac{r}{l} \right)^2 + \frac{1}{16} \left(\frac{r}{l} \right)^4 + \dots \right] \cos 2\omega t \\
& + \left[-\frac{1}{64} \left(\frac{r}{l} \right)^4 + \dots \right] \cos 4\omega t \\
& + \dots
\end{aligned} \tag{10}$$

The coefficients could be expressed in the form of Elliptic integrals if the assumption of small r/l is not made, but the series still consists of a constant, a term at the fundamental piston frequency and the odd harmonics of the fundamental frequency (2ω is the first harmonic of the fundamental frequency ω). This series clearly points out that harmonics of the fundamental frequency will be seen in the experiments. In actuality, all of the harmonics are seen, not just the odd harmonics. This may be due to looseness in the bearing or nonlinearity in the wave propagation.

Flow Measurements

Mass Flow Measurements. Mass flow measurements were carried out routinely whenever the chamber was operated and proved to be extremely useful as a quantitative measure of the phenomena occurring. The carbon dioxide gas leaving the chamber passed through a rotameter type flow meter. Three flow meters, 0 - 50 SCFH, 0 - 100 SCFH and 0 - 200 SCFH, manufactured by Dwyer Instruments were used, depending on the flow rate. All of these were calibrated for use in air and were corrected to read the flow rate for carbon dioxide at non-standard conditions.

Pressure Measurements. The chamber was instrumented with both a water manometer, to measure pressures in steady state operation, and a Kistler pressure transducer, model 606L, to measure the oscillating pressures that occurred when the piston was operated. The pressure transducer was initially located on the side wall of the dry ice section and communicated to the main chamber via an opening around the head end window. This arrangement, it was learned, resulted in a somewhat reduced pressure reading. After this problem was discovered, the transducer was mounted in a plate replacing the head end window. This became the nominal location for the transducer. A mounting hole was also provided on the chamber side wall downstream of the side window. When the chamber was operated with the dry ice section in the center of the chamber a second transducer was located at one of the two side wall locations along with one at the head end of the chamber.

Hot Film Anemometry. Hot film anemometry was used to determine the spectrum of the velocity oscillations in the chamber. For this purpose, the hot film was

operated uncalibrated. A single component probe, TSI model 1210-60, was used with a TSI model IFA-100 analyzer. The velocity signal from this system was displayed on a Nicolet digital oscilloscope and spectrum analyzed using an HP 3582A Spectrum Analyzer. As a result of discussions with TSI, no attempt to calibrate the hot film probe was undertaken, since it could not compensate for the strong thermal effects that occurred due to the extreme temperature gradients in the chamber. The hot film anemometer could not be stably operated when the infrared lamp was in operation due to the additional radiative effect. Because of this limitation, all hot film data was taken with the infrared lamp off.

Laser Doppler Anemometry. A Dantec Laser Doppler Anemometer (LDA) 3-beam, two component system with a high power, 5-Watt, Argon-ion laser was used in the backscattering mode to measure particle velocities in the chamber. This 3-beam system is capable of measuring two components of velocity simultaneously and is recommended for applications where a detailed study of turbulence parameters is required. Separation of the two components of velocity is achieved by color, using the green and the blue line of the Ar-ion spectrum. The high laser power ensures optimum signal to noise ratio. This two component system is very compact and rotation of the beam plane is possible so that the components of velocity being measured can be varied. Adjustment of the laser beam waist is also possible to ensure optimum light intensity in the probe volume. Frequency shift is included so that full resolution of reversing and highly turbulent flows is possible (this option has not been used in the chamber measurements).

The probe volume was placed several millimeters above the center of the dry ice half way between the ends of the dry ice and half way between the walls of the chamber. The probe volume location is adjustable from near the surface of the dry ice to 6 mm above the surface. Measurement time and the number of samples were variable. The two components of the velocity are obtained for each sample. The mean, RMS, flatness and skewness of both velocity distributions are available as well as cross correlations between the two components.

The computer software supplied with this system is designed to be used in a flow in a rotating machine (where a periodic flow would occur). Using this software, velocity data is collected over many cycles. The time each data point was obtained, relative to a timing signal which occurs once per cycle, is recorded. After a full set of data is obtained the data can then be collected into groups determined by the time when it was obtained, relative to the timing signal. Each group of data was obtained during a given fractional period of the cycle or rotation. These fractional periods of the rotation are referred to as sectors or bins and their width is given in degrees (for example, if the sectors were 10° wide there would be 36 in the cycle). The width of a sector can be set in the software. The velocity data in each sector is viewed as if it was taken at the same phase of the cycle and analyzed as such. This phase averaging approach is necessary if only a very limited number of data points are obtained during a cycle of the flow.

RESULTS

Steady Flow Rates

The steady flow rate from the dry ice (or the injection rate) plays a key role in the unsteady data obtained. This steady mass flow rate was determined using the flow meters discussed in Section 2.4.1. These flow meters were calibrated for air at standard conditions and the readings corrected for the gas being carbon dioxide at non-standard conditions. The chamber operated, at most, a few centimeters of water above normal atmospheric pressure in Salt Lake City, 0.85 Atmosphere, and the flow exited the chamber at a temperature of about 23°C. Figure 7 shows the flow rates obtained with the original white insulating reflector on the commercial infrared source and for the gold plated reflector. Note that in both case the flow rates are extremely small, about 6%, of the theoretical value (0.00305 m³/sec) given in Section 2.2. Thus maximum values of all of the flow parameters discussed in that section are reduced to about 6% of the previous values. The maximum injection velocity is of the order of 1 cm / sec. The gold plated reflector increases the flow rates by as much as 10% beyond the white insulating reflector, but the values remain quite small.

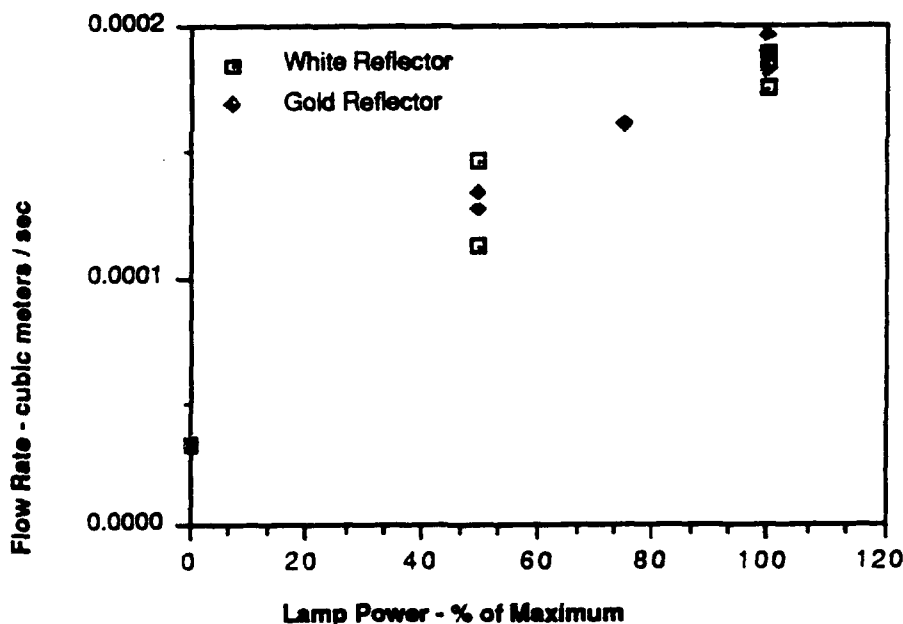


Figure 7
Steady flow rate from the dry ice as a function of lamp power and the type of reflector used, maximum input power to the lamp power supply is 4.8 kW

In an attempt to increase the absorption of the infrared radiation and sublimation rate, flow rate tests were carried out using dry ice to which either water or carbon black had been added. These additives increased the sublimation rate by as much as a

factor of four in small scale experiments [27]. To add such materials to the dry ice required that the dry ice be ground into small particles, the material added and the combination recompressed into a block. This composite material has sufficient strength for small scale test but frequently broke when large pieces were used. In the chamber no significant increase in flow rate was detected comparable to that in the small scale test. No explanation for this has been determined.

Acoustic Characteristics

The fundamental natural frequencies of the chamber at each of six different conditions have been determined by driving the piston at near half of the fundamental natural frequency and monitoring the head end pressure output with a spectrum analyzer and a digital oscilloscope. The piston frequency at which the first harmonic term of the pressure spectrum maximizes is taken as one half of the fundamental natural frequency. The overall pressure amplitude also reaches a local maximum at this frequency as recorded with the oscilloscope.

The six conditions considered are: 1) the dry ice section at the chamber head end with dry ice and the infrared lamp on at full power (This is denoted as the HDILO case, (head end, dry ice, lamp on)); 2) same configuration as 1 but without infrared radiation (no lamp, HDINL); 3) the section at the head end position, but with a flat metal plate replacing the dry ice, HFP; 4) the dry ice section near the chamber center, with dry ice and the infrared lamp on at full power, CDILO; 5) dry ice section near the center with dry ice and no radiation, CDINL; 6) the section near the center but fitted with the flat plate, CFP.

The speed of sound in each operating condition was determined by examining the spectrum outputs of the pressure signals at two different locations, while operating the piston at one half of the natural frequency. By knowing the ratio of pressure amplitudes at the fundamental natural frequency (which happen to be the first harmonic of the piston motion in this case) and the distance between the two transducers, the speed of sound can be calculated using linear acoustic theory [28]. There are two reasons for running the piston at the half of the resonant frequency for the measurement. First, the fundamental mode of oscillation of the tube is excited by the piston first harmonic and is dominant over the oscillation at the fundamental driving frequency. In this situation the effect of simple compression due to piston displacement is minimized. Second, the excitation of the fundamental mode is still quite weak under this condition and linear acoustic theory can be applied.

Table 2 lists the experimental fundamental natural frequencies and speeds of sound obtained using the methods stated above. Also listed are the actual chamber length, L_a . (Note that this data was taken before the vibration isolation coupling was installed and reflects a shorter tube than that described in Section 2.3) and the effective length, L_e , calculated from the frequency, sound speed and assuming a closed end tube.

Table 2. Experimental Natural Frequencies and Speeds of Sound

Case	Freq. (Hz)	a_0 (m/sec)	L_a (m)	L_e (m)
CDILO	70.0	279.5	2.0	1.997
CDINL	67.2	268.4	2.0	1.997
CFP	68.4	274.9	2.0	2.009
HDILO	65.5	161.4	1.88	1.232
HDINL	67.2	148.7	1.88	1.109
HFP	69.6	212.9	1.88	1.529

It can be seen that for the cases where the dry ice section is located near the chamber center the results are very consistent as indicated by the very small differences between L_a and L_e . The differences in the speeds of sound result from the differences in the mean temperatures of the chamber. Since the chamber is purged with room temperature CO₂ gas before each run, the mean temperature in the CFP case is same as room temperature. The mean temperature in the CDINL case will be lower since the sublimated CO₂ gas has an initial temperature of -78°C; therefore in Table 2 a smaller speed of sound is expected. On the other hand, in the case of CDILO, the temperature of the sublimated CO₂ gas rises sharply due to the heating of the gas in the presence of the infrared radiation. The chamber wall temperature also increases. The overall mean temperature in this case is higher than the CFP case and results in a higher speed of sound. The shift in the natural frequencies results from the difference in speeds of sound.

The same explanations fail when applied to the cases with dry ice section located at head end, where large differences were observed between the actual and effective chamber length. The speeds of sound with dry ice (both with the infrared light both on and off) suggest that the mean chamber temperatures are well below the sublimation temperature of dry ice (-78°C), which is not possible. The mean chamber temperature should be largely determined by the experimental conditions and have only a very weak dependence on the actual location of the dry ice section. The speeds of sound would be expected to be very similar to those obtained with dry ice section near chamber center. By using the same values of speed of sound as CFP, CDILO and CDINL, correspondingly, a new set of values of L_e can be calculated and are listed in Table 3. It is observed that the effective lengths of the chamber are greater than the actual length when the dry ice section is located at head end.

This phenomenon is not very difficult to understand. Although, an effort has been made to have the aluminum plate fit snugly in the dry ice opening, small gaps exist between the aluminum plate and the section wall. There is also a space under the aluminum plate. These facts make the aluminum plate behave like a porous surface. Dry ice is clearly more porous than an aluminum plate and the gaps between dry ice block and chamber wall are also greater, since dry ice will sublime as soon as it comes in contact with the aluminum walls, which are initially at room temperature. When infrared radiation is applied to the dry ice surface, localized higher sublimation has been observed due to uneven seeding of water particles. These intense locally

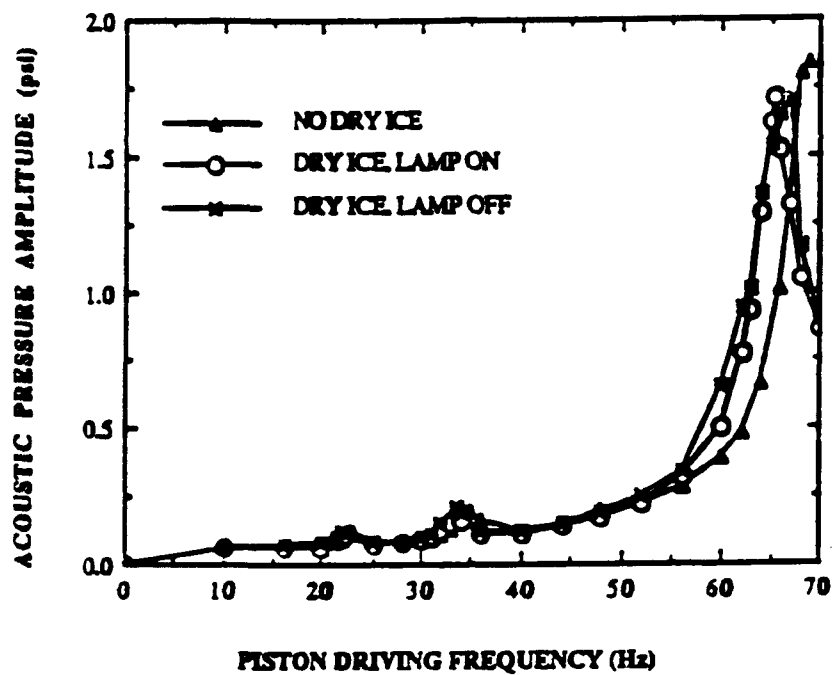
Table 3. Corrected Experimental Natural Frequencies and Speeds of Sound

Case	Freq. (Hz)	a_0 (m/s)	L_a (m)	L_e (m)
CDILO	70.0	279.5	2.0	1.997
CDINL	67.2	268.4	2.0	1.997
CFP	68.4	274.9	2.0	2.009
HDILO	65.5	279.5	1.88	2.134
HDINL	67.2	268.4	1.88	1.997
HFP	69.6	274.9	1.88	1.975

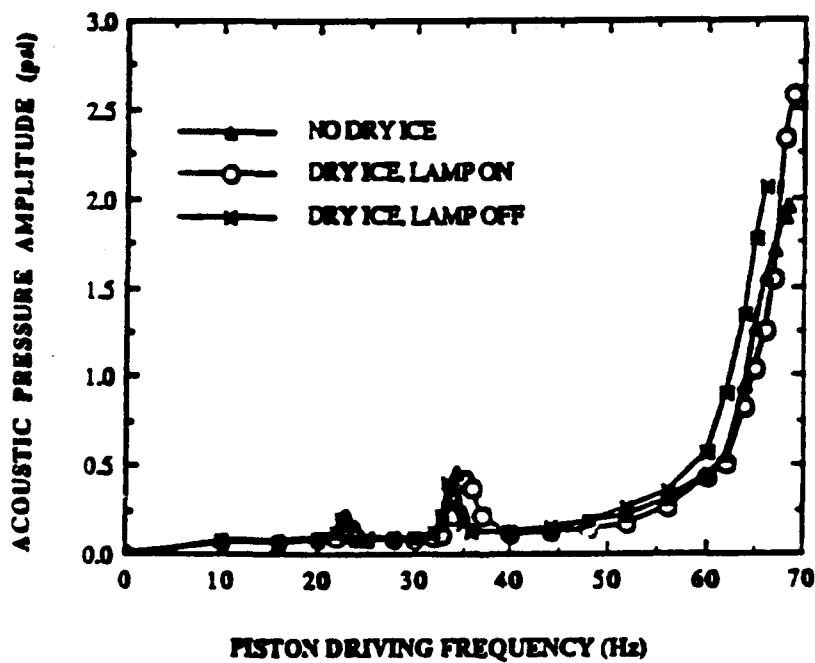
high sublimation rates create small holes on the dry ice surface. As a result of these holes, the surface of dry ice with the infrared radiation source on is more porous than a dry ice surface that has not been exposed to infrared radiation. When pressure varies over a porous surface, the surface will allow the gas to expand into the available space below the surface and tend to damp out the pressure disturbances. When a porous surface is placed near the center of the chamber, its effect on the acoustic waves is very small since the pressure does not vary much due to the small acoustic pressure amplitude at the center, when the fundamental acoustic mode is excited. When this same porous surface is moved to the head end of the chamber, where large pressure variation is expected due to large acoustic pressure amplitude, strong effects on the acoustic waves are expected. First, the acoustic pressure amplitudes are expected to be smaller due to the damping, which is exactly the case and will be discussed later in details. Second, since this damping mechanism is only present over certain portions of the chamber, the resulting pressure gradient over the porous dry ice surface is greater than that over a solid surface, which possibly explains why the effective length of the chamber is greater than the actual length when the dry ice section is located at head end. The more porous the surface, the stronger the effect.

Figure 8 shows the acoustic pressure amplitudes measured at the head end versus the piston driving frequency for the six different configurations. Small peaks have been observed near 23 Hz and 34 Hz. These peaks occur due to the excitation of the first acoustic mode of the chamber by the second or first harmonic of the piston motion. Figure 9 shows two typical pressure waveforms observed at these frequencies. A sharp increase in the pressure amplitudes is observed near resonance for all cases, as expected. Full resonance for the cases of CFP, CDILO, CDINL and HFP can not be obtained with the present electric motor. The power output of the electric motor is too small to overcome the pressure associated with the shocks that occur in these cases. The data collection for the HDILO and HDINL cases stops at about 70 Hz, because of fear of overheating and the limits on the piston rotation speed.

In the CDILO, CDINL, HDILO and HDINL cases, no excitation of the second or higher acoustic modes has been observed, except near full resonance, where excitations of all acoustic modes has been observed. The amplitudes of these higher acoustic modes decreases very rapidly with increasing frequency due to the reasons



a)



b)

Figure 8
 Acoustic pressure amplitude at the upstream end of the chamber as a function of piston frequency: a) dry ice section upstream. b) dry ice section near the chamber center

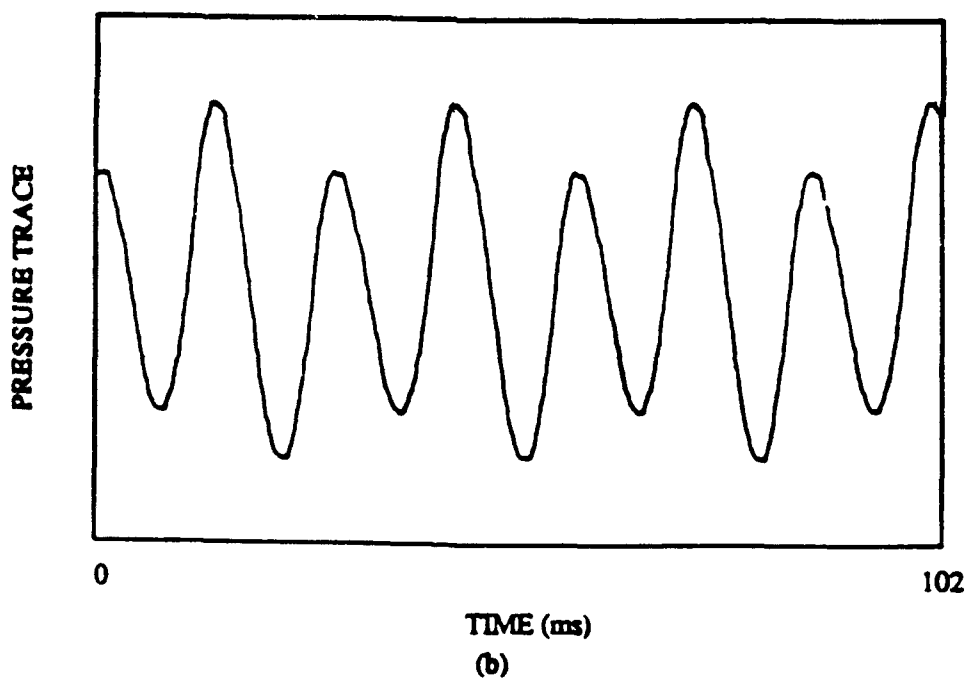
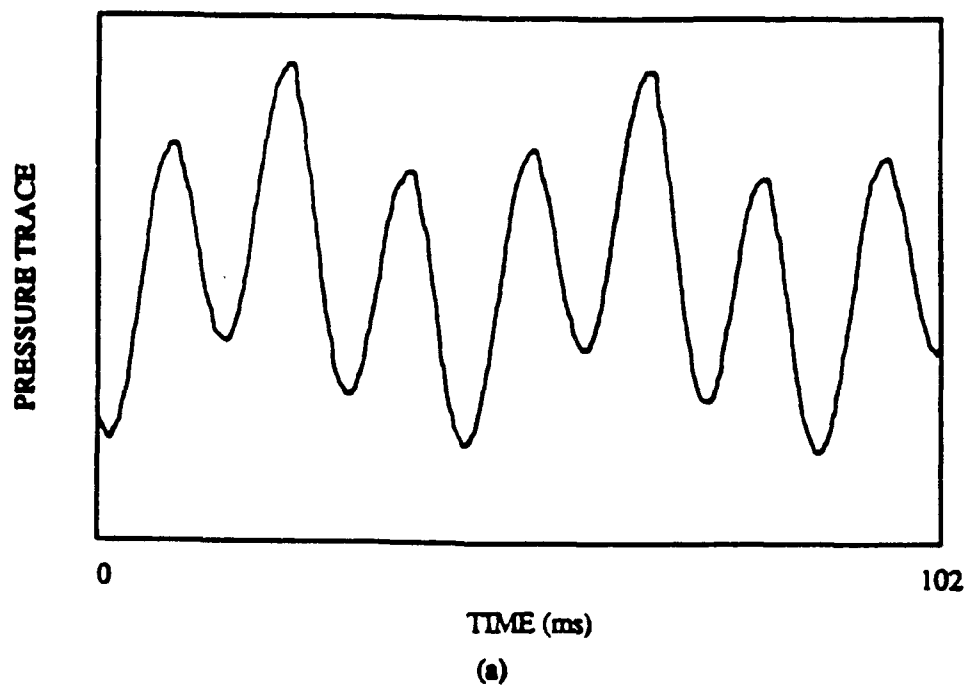


Figure 9
 Acoustic pressure amplitude at the upstream end of the chamber as a function of time for the piston being operated at: a) 22.8 Hz. (one-third of the resonant frequency); b) 34.2 Hz (one-half of the resonant frequency), resonant frequency is at about 68 Hz. with no dry ice in the tube

given in Section 2.3, and the contribution of these higher modes to the total acoustic field is small. In the CFP and HFP cases, excitation of higher acoustic modes (up to the sixth mode) have been observed when the piston is operating at fractions of these frequencies. No excitation of transverse acoustic mode frequencies has been observed in any configuration. In this case an assumption of one-dimensionality of the acoustic field (or more correctly that all significant acoustic velocities are in the longitudinal direction) inside the chamber is reasonable.

Nonlinear, steep-fronted waves (Figure 10) have been detected by the head end pressure transducer near resonance for all cases. The degree of steepness and the magnitude of the maximum shock vary from case to case.

A close examination of Figure 8 shows that the acoustic pressure amplitudes for the cases with the dry ice section near the chamber center (part b) are all greater than

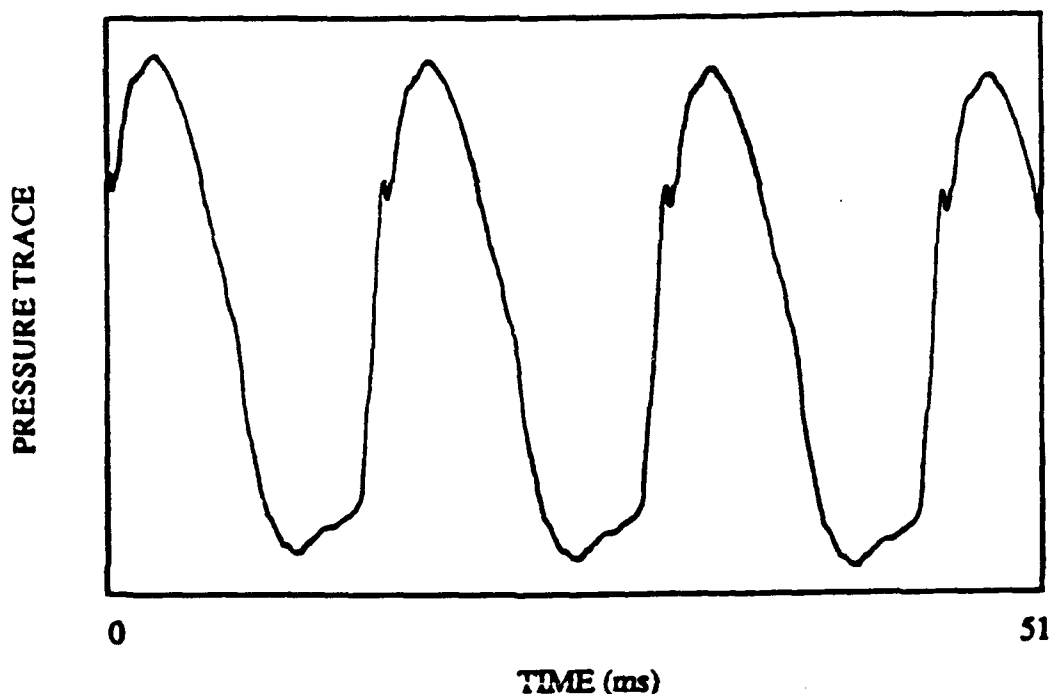


Figure 10
Acoustic pressure amplitude at the upstream end of the chamber as a function of time with dry ice located near the tube center and the piston being operated at the tube resonant frequency

their counterparts with dry ice section at head end (part a). This observation is in agreement with the arguments in the previous paragraphs.

Another observation, an extremely interesting one, is that when the dry ice section is located near the center the acoustic pressure amplitude near resonance is greatest in the CDILO case, smaller in the CDINL case and smallest in the CFP case. When the dry ice section is located at the head end, this order is almost reversed. The pressure amplitude is largest in the HFP case and smaller and about equal for both the HDILO and HDINL cases. This phenomenon can not be explained using the simple argument presented above. An acoustic driving mechanism, probably related to the velocity oscillation and the dry ice sublimation process, must exist.

The amplitude of the acoustic oscillation is clearly determined by the driving and damping mechanisms present in the system. The driving mechanism in the CFP and HFP cases is clearly the piston motion. The nonperfect fitting of aluminum plate in the chamber provides a damping mechanism along with viscous effects. In the cases where dry ice is used, the driving mechanism is again the piston motion. There are additional damping mechanisms when dry ice is in the chamber. First, the effect of nonperfect fitting of the dry ice block with the chamber will provide an acoustic energy sink, which is expected to be stronger than in the cases with the aluminum plate. Second, the viscous effects, which are expected to be slightly smaller for the cases with dry ice and no infrared radiation, than in the aluminum plate cases, due to lower viscosity associated with lower temperature, while the viscous damping will be slightly higher than in the aluminum plate cases when dry ice and infrared radiation are both used, due to the slightly higher viscosity with higher temperature. A third possibility is flow turning, the sublimated gas enters the chamber with a velocity perpendicular to the longitudinal direction and obtains acoustic excitation as it turns towards the downstream direction to exit the chamber. The need to acoustically excite this entering gas acts as an acoustic sink to the gas in the chamber. As will be discussed more extensively in the following section, the sublimation rate of the dry ice has been observed to increase with the increasing acoustic disturbance. It is then expected that damping due to the flow turning effect would also increase with the increasing acoustic oscillation. This flow turning damping effect should also be stronger when the dry ice section is located near the center of the chamber, since the acoustic velocity is greater near the chamber center. Finally, the gas exiting the downstream orifice will carry part of the acoustic energy with it. Due to this loss of acoustic energy, one would expect the pressure amplitudes in the cases with dry ice to be always less than the cases with the aluminum plate. The opposite finding here does suggest that one has to look further for other driving mechanisms.

A velocity type of coupling mechanism is more likely to be the driving force. When the dry ice is located at the head end, a velocity node, the velocity amplitude is relatively small even at full resonance. The balance between velocity coupling driving and the combined damping effect of flow turning, surface admittance and viscosity results in a pressure amplitude less than that with an aluminum plate. When the dry ice is moved near the center of the chamber, the velocity coupling type driving increases, due to the increased velocity amplitude, while the surface damping effect decreases with the decreased pressure amplitude. This results in the dramatic increase in the acoustic pressure amplitude that is observed in the cases with dry ice.

This explanation should also depend on the sublimation rate. The sublimation rate is higher when infrared radiation is supplied to the dry ice. In this case the acoustic pressure amplitudes are both expected and observed to be higher than in the cases without radiation. This effect occurs despite a potentially higher flow turning loss accompanying the higher sublimation rate.

Acoustically Generated Turbulence

Transition to Turbulence.

Flow Visualization Results. Flow visualization and hot film techniques have been used to examine the flow over the dry ice surface in all cases with external radiation. With the flow visualization a standard video system with a 30 Hz frame rate has been used to record the flow field. A videotape is available showing most of the flow patterns described below.

Under steady state operating conditions, i.e., no acoustic oscillation, a fairly uniform layer of fog can be clearly observed to form over the dry ice surface as soon as the infrared radiation is applied. This layer of fog appears to be a collection of suspended water droplets and occurs at a distance of about 3 to 5 mm above the dry ice surface. There is a distinct clear region between the fog layer and the dry ice surface. This layer of fog results from the water particles premixed within the dry ice during its manufacturing process. This has been verified by using dry ice produced with no added water and the fog was nearly eliminated. This premixed water is necessary in order to bind the dry ice together into an easily handled material. About 1% (by weight) of water is believed to exist in the dry ice by the manufacturers. The fog layer provides an extremely convenient means of visualization in this study. Jets of fog sometimes are observed to shoot through the main fog layer and then fall back into the uniform layer. These jets are believed to be caused by local high concentration of water particles in the dry ice. In the wave length range of the infrared radiation source used (1.2μ peak radiation), water ice absorbs more energy than the dry ice. If a crystal of water ice is located near the surface it rapidly heats up producing a jet. The temperature at the center of the fog layer was measured to be about 0°C with a shielded thermocouple. As the temperature of the dry ice surface is -78°C , a strong temperature gradient must exist above the dry ice surface. This temperature gradient provides a stable flow condition.

When an acoustic disturbance is introduced over the dry ice surface at low frequencies, the layer of fog is observed to pulsate up and down uniformly in response to the simple compression of the piston. As the piston frequency increases, the amplitude of the fog layer pulsation decreases. The layer eventually becomes visually stationary when the piston reaches a frequency of about 16 Hz. The fog layer remains stationary until a critical value of the acoustic frequency (or related disturbance amplitude) is reached. The flow within the chamber, before the threshold condition, definitely appears laminar and stable. Figure 11 shows a stable fog layer. The values of this critical acoustic oscillation amplitude and frequency are different for different dry ice locations.

In the CDILO case, instability is observed to occur within the fog layer when the piston is beginning to approach one third the chamber fundamental natural frequency (23.3 Hz). At the initiation of this instability, the fog layer exhibits a pattern of gradually varying peaks and troughs, in both space and time, typical of a wave-like pattern. The amplitude of this wave-like pattern increases as the piston frequency further approaches one third of the fundamental natural frequency (and the acoustic excitation becomes stronger). This wave-like pattern also exhibits a propagational behavior very similar to that of water waves. The "waves" propagate in both upstream and downstream directions from the center of dry ice section. The waves associated

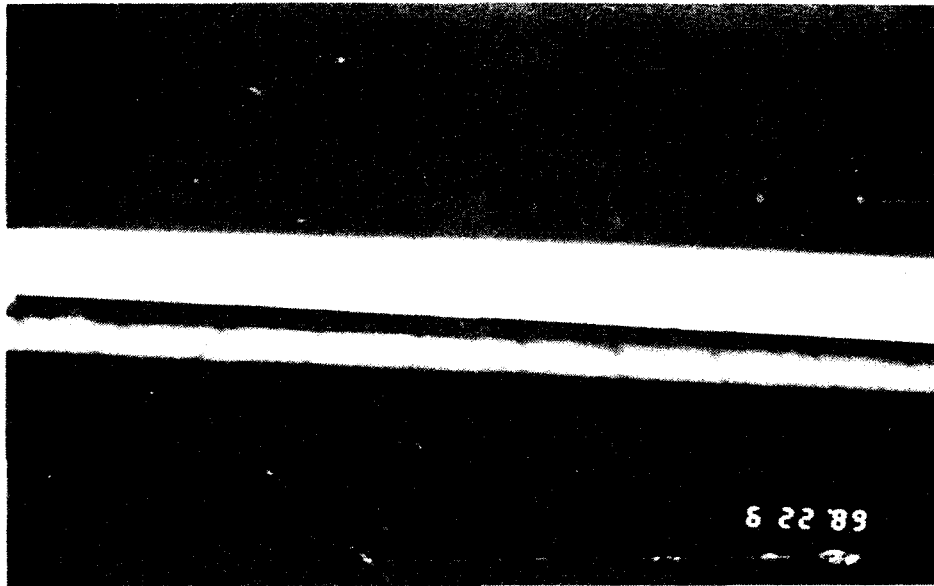


Figure 11
Steady fog layer that occurs with no acoustic excitation

with the fog layer are extremely two-dimensional with the wave front observed to be very uniform across the width of the chamber. The wave-like motion within the fog layer is strongest when piston is operating at the one third of the fundamental natural frequency. The propagation of the waves remains very smooth and two-dimensional. The flow, however, still appears to be laminar, although near the transition to turbulence. At this condition no clear indication of mixing within the flow has been observed. Figure 12 shows the type of wave motion observed with the fog layer.

The amplitude of the wave motion next decreases with increasing piston frequency, likely due to the decrease in the acoustic oscillation amplitude. At 25 Hz, the fog layer regains its stability and appears to be stationary again until piston frequency approaches one half of the natural frequency of the chamber (35 Hz).

At about 30 Hz, the wave-like instability in the fog layer returns. The amplitude of the fog wave motion again increases as the piston speed and acoustic amplitude increase. At about 33 Hz, weak burst of particles can be observed to leave the surface indicating local high intensity instability. The smooth two-dimensional wave propagation no longer occurs. The waves break in a manner very reminiscent to the breaking of high amplitude water waves. The process of transition to turbulence is believed to be taking place. When piston speed is increased further, with a corresponding increase in the acoustic oscillation amplitude, a very interesting phenomenon is observed. The breaking wave fronts rise vertically, forming a series of plane fog layers in the vertical direction which is amazingly uniform across the width of the chamber. This type of wave form also propagates in both upstream and

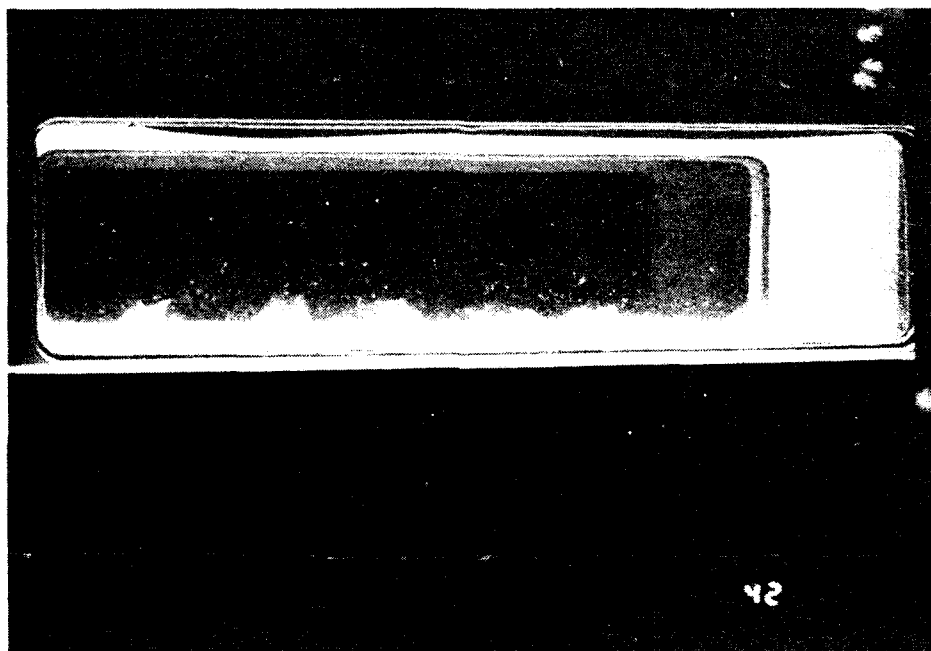


Figure 12
Two-dimensional wave-like motion of the fog layer that occurs
with the piston operating at 23 Hz and dry ice near the center of
the tube with the infrared lamp on

downstream directions. The tip of the fog slightly inclines in the direction of the propagation and rolls forward as it travels, forming transverse vortices. As the piston speed is increased to within about 0.5 Hz of one half of the natural frequency of the chamber, the fog layer motion becomes chaotic and three-dimensional. This flow is believed to be turbulent. At one half of the fundamental natural frequency, the fog is so dispersed by the turbulent mixing that it is barely visible.

Further increase in the piston driving frequency will cause the fog layer to exhibit flow patterns in the reverse order of that observed when approaching half of the natural frequency. The fog layer never returns to the totally stable condition. The

water wave type of motion persists. At about 50 Hz, transitional behavior is observed again within the fog layer. The flow becomes three-dimensional and mixing occurs. The chaotic motion becomes more intense with any further increase in the piston frequency. At about 60 Hz, the fog layer is no longer visible due to increased mixing. The presence of an increasing number of particles ejected from the dry ice surface indicates a very turbulent motion within the flow above the dry ice surface.

A possible explanation of these ejected particles, which appear to be ejected in random directions, is that they result from turbulent bursts associated with "wall" turbulent shear flow. The assumption made here is that the turbulent structure in this experiment is very similar to that in nontranspiring surface case, where turbulent bursting, category 3 as discussed in the introduction, has been observed. Hino, et al. [21,22] suggested this flow to be very similar to that in one-directional, turbulent shear flow at a wall. In steady wall shear flow turbulent bursting results from stretching of horseshoe-shaped vortices (see Hinze [29]). Ejection of low momentum fluid away from the wall boundary is observed to occur with the bursting. A stronger basis for the assumption made here will be discussed later in the hot film anemometry section. Although randomly ejected from the surface, most of the particles appear to take paths inclining towards the downstream direction. The particles also tend to follow the acoustic oscillations as they leave the surface, exhibiting a longitudinal sinusoidal motion along the main trajectories. The particles can also be seen to bounce off the side walls of the chamber making it very difficult to follow the particle trajectories for long distances.

Secondary motion of the particles can also be observed near the dry ice surface. Particles are seen to move in the downstream direction along the surface, towards the pressure antinode. This phenomenon likely indicates the influence of the acoustic streaming [30,31]. Large pieces of dry ice occasionally break off from the dry ice surface due to strong shear stress. These large pieces of dry ice are not ejected from the surface nor attempt to follow the acoustic oscillation as the small particles do. The large pieces of dry ice do move along the surface in the direction of the acoustic streaming. The chaotic motion of the small dry ice particles appears to fill the whole dry ice section at full resonance. What appears to be a pair of large spiral vortices can also be observed to travel downstream from time to time.

In the HDILO case the initial instability does not occur within the fog layer until the piston frequency is very close to one half of the fundamental resonant frequency, 32.7 Hz in this case, most likely due to the decreased gas motion parallel to the dry ice surface since the dry ice is located near the velocity node. At 32.7 Hz, the fog layer only exhibits a weak water wave type of motion, indicating the weakness of the instability. The flow remains laminar. The instabilities quickly disappear when the piston speed is higher than one half of the fundamental frequency and the fog layer becomes visually stationary again.

The transitional behavior occurs when the piston speed is about 52 Hz. Weak disturbances cause the water wave type of motion in the fog layer. The propagation of wave motion, however, is not very two-dimensional and planar but rather appears to be radially outward from the center of the dry ice. Further increase in the piston frequency and acoustic amplitude causes the fog layer motion to become three-

dimensional, random and swirling. Puffs of fog can be seen to be generated near the surface occasionally, possibly an indication of turbulent bursting. The fog layer becomes invisible at about 60 Hz due to intense mixing. Visualization beyond this point again relies on the particles ejected from the surface.

The motion associated with the particles in this case is very similar to that of CDILO case. The major difference is the direction of the secondary particle motion near the surface. The particles, and the occasionally observed large dry ice pieces, are seen to travel in the upstream direction. This is consistent with a secondary motion produced by acoustic streaming, where a net flow circulation occurs with the flow near the surface moving from the velocity antinode towards the pressure antinode which is at the head end of the chamber in this case. The flow near resonance is again very chaotic and turbulent.

When the dry ice is located at the head end, the effect of surface roughness is very evident. The flow pattern for a rough surface is different from that described above for a smooth surface. A rough surface can be easily achieved by letting a piece of smooth dry ice run at the full resonant condition for a short time. Figure 13 shows typical surfaces of a dry ice block before and after an experiment. When the surface is rough, instability can be observed to occur when the piston is operating near one third of the natural frequency.

Near one third of resonance, approximately 23 Hz, the fog layer exhibits a pattern with randomly distributed small peaks. These peaks are very smooth and appear to result from overshooting or jetting of the fog due to a local high sublimation rate. No wave-like motion is seen to propagate over the surface. The fog jets are fixed in location. Each jet seems to form a small vortex as the tip of the jet moves towards downstream direction and falls back toward the surface at the same time. The downstream motion is necessary for the gas to leave the chamber, while the falling is the result of gravity as the water particles in the jet try to find their equilibrium position. No interference between neighboring jets has been observed. These weak jets disappear when piston is running slightly higher than one third of the natural frequency, resulting in a flat fog layer.

As the piston frequency approaches 32.7 Hz, the jets of fog reappear. Again the distribution of the jetting over the dry ice surface is very random. It is very possible that the jetting occurs at the same locations as at one third of the resonant frequency. No wave-like behavior has been observed in the fog layer, even at 32.7 Hz. As the piston frequency is increased, approaching 32.7 Hz, the height of the jetting increases, indicating strong response of the sublimation process to increasing acoustic oscillation amplitude. At 32.7 Hz, the tips of the jets do not fall back toward the dry ice surface but rather move straight towards the downstream direction. Transverse motion has been observed to be superimposed upon the fog layer motion. The jets start to interfere and mix with each other. The flow is weakly turbulent.

Further increase in the piston speed results in a decrease in the intensity of the motion associated with the fog jets. The height of the jets also decrease. At about 50 Hz, the intensity in the jetting increases again. The motion becomes three-dimensional and random, indicating transitional behavior approaching turbulence.

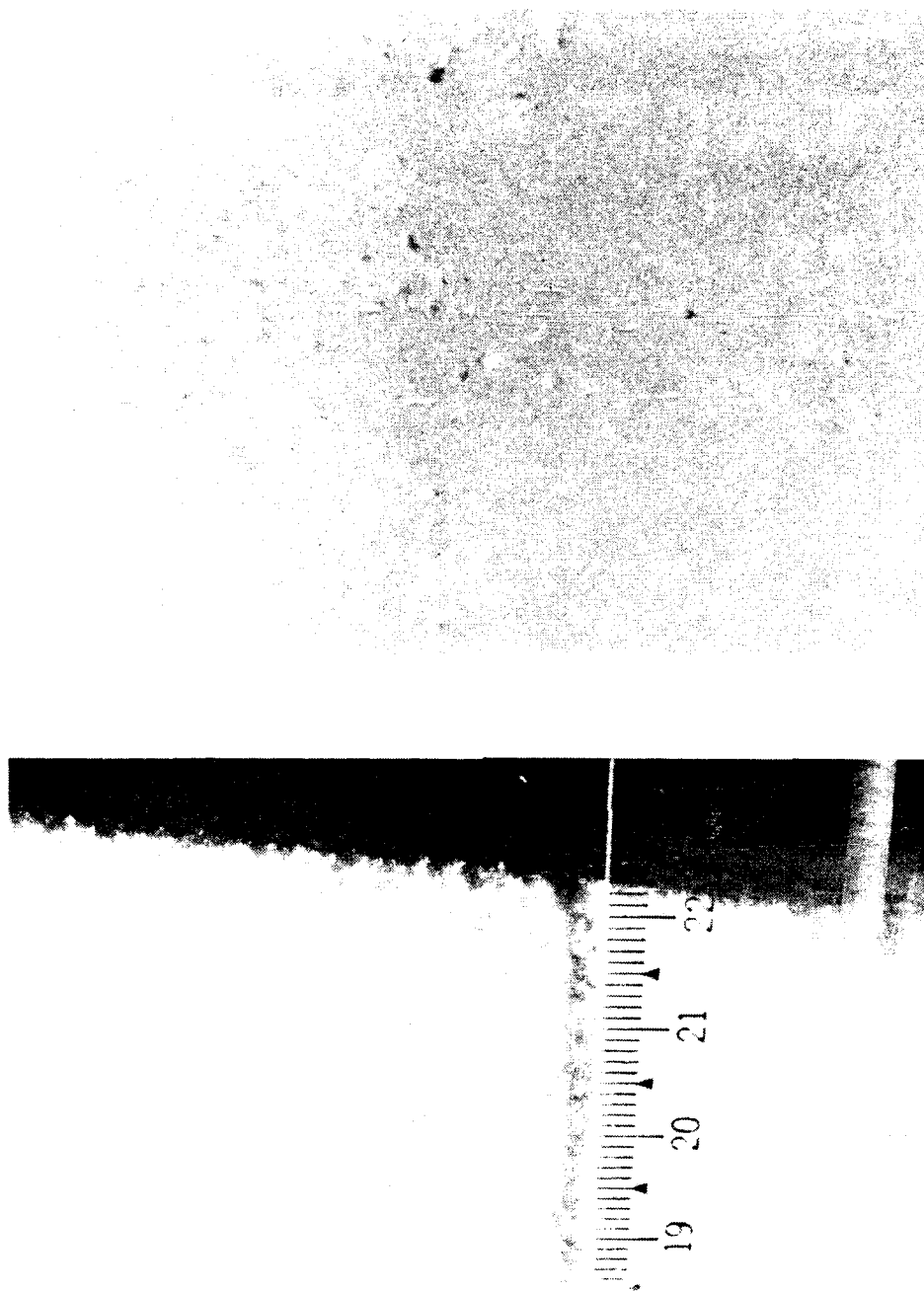


Figure 13
Comparison of (above) the smooth dry ice surface before an experiment and (below) the rough surface after the experiment

When the piston speed is higher than 58 Hz, the fog is no longer visible. The motion associated with the ejected particles is very similar to that when the surface is smooth.

The distinguishing characteristic of the flow pattern in this case is the dominance of the local instability. The instability is very localized, random in location and does not propagate into neighboring regions as compared to the highly organized and propagative flow pattern observed with dry ice located near the chamber center. It is believed that the difference in the flow pattern is caused by the difference in the shear stress. The strong shear stress near the center produces highly organized motion, while the weaker shear stress at the head end allows the instability to be localized and random. Another indication of this type of mechanism is the fact that surface roughness appears to make no significant difference in the flow pattern observed when dry ice is located near the center.

In all situations, whenever there is an indication of approaching instability or of instability in the flow motion, an increase in the mean sublimation rate is observed, in addition to an increase in the mean chamber pressure. Enhanced sublimation has been observed even while the flow appears to be laminar.

Experiments conducted with the piston operating at full resonance show that the surface of the dry ice regresses faster where the acoustic velocity is expected to be higher. Therefore the upstream end of the dry ice surface in CDILO and CDINL cases regresses faster than the downstream end, while the opposite happens in HDILO and HDINL cases. Figure 14 shows the change in the thickness of a dry ice block before and after an experimental run at full resonance. If the dry ice surface is lower than the chamber floor, which sometimes happens, vortices could be shed at the interface of the dry ice and the chamber floor. Vortex shedding and the resulting heat transfer could enhance the effect observed. It is very desirable to have the center of the dry ice coincide with the center of the chamber. This has not been achieved in the current experiment, however. The mean flow velocity in this experiment is relatively low and the vortex shedding resulting from the mean flow will likely have a small effect. Previous experiments by Crump and Price [3, 4] did suggest the same phenomenon, while vortex shedding does not play a role in their experiments.

Visualization has been attempted with CDINL and HDINL cases. However, due to lack of a light source and the presence of only small amount of fog, visualization is not very effective. The limited results do tend to confirm the general trends observed for their counterparts with infrared radiation.

Hot Film Results. Hot film anemometry is used to further verify the occurrence of turbulence in the flow. There are several ways to judge the transition to turbulence based on hot film velocity measurements. The primary method used in this experiment is to examine the spectrum of the hot film output.

A broad band spectrum indicates the occurrence of turbulent flow. Most of turbulent energy is carried by large scale eddies and the first indication of turbulence would be the appearance of a flat spectrum at low frequency. It is particularly important to examine the spectrum in the range of 0-100 Hz (This range actually extends to 10² Hz on the spectrum analyzer, a fact that sometimes results in one more

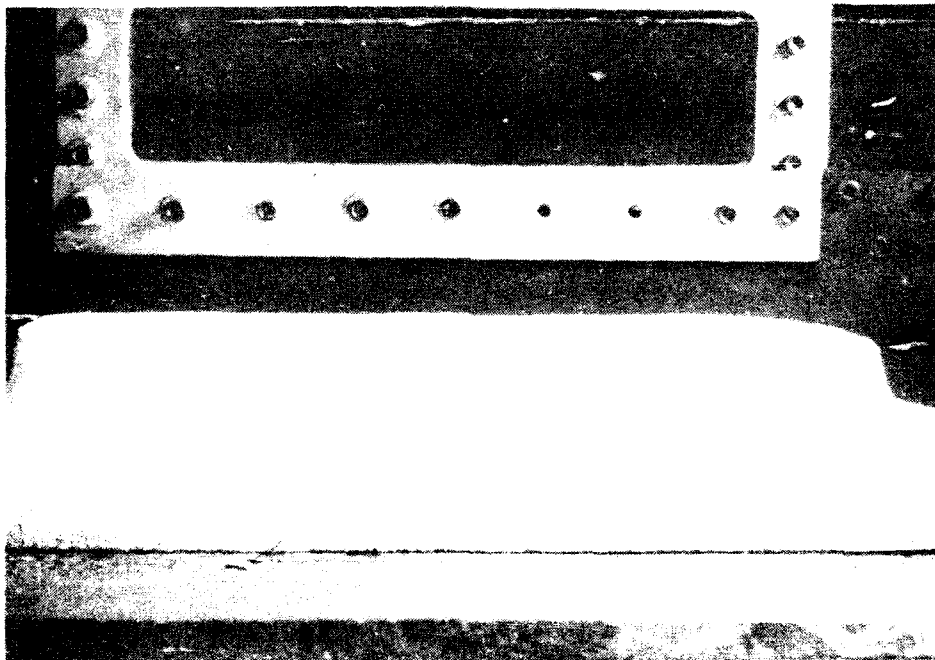
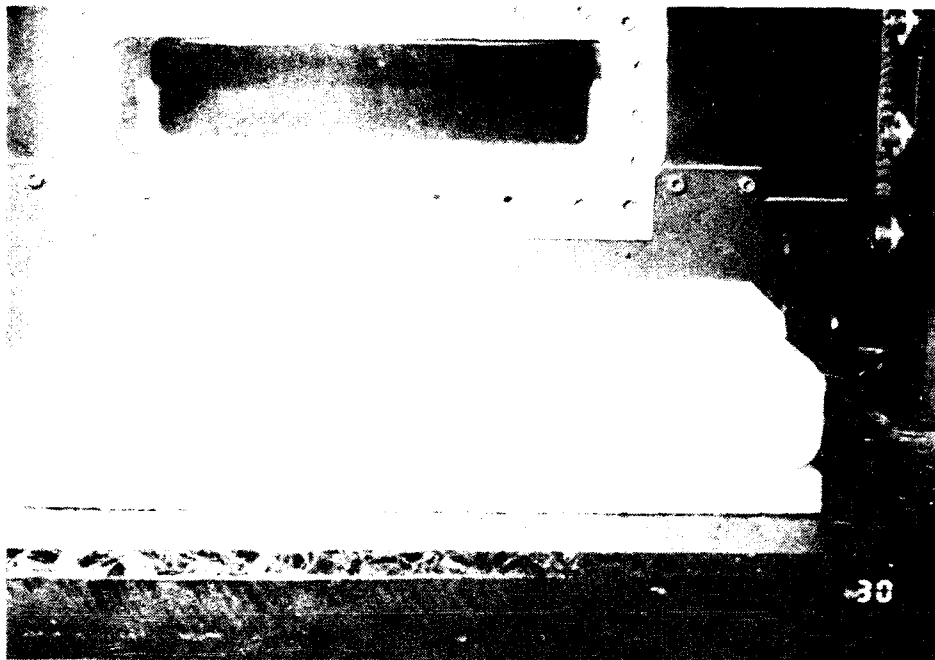
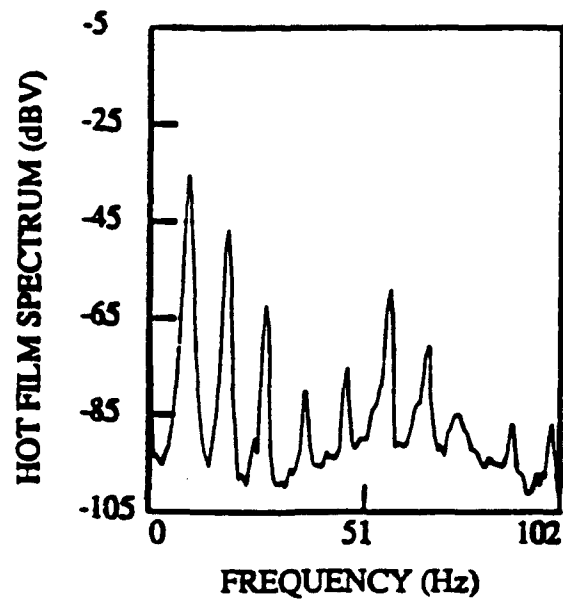


Figure 14
Change in the thickness of the dry ice block during an experiment:
(above) before an experiment; (below) after an experiment

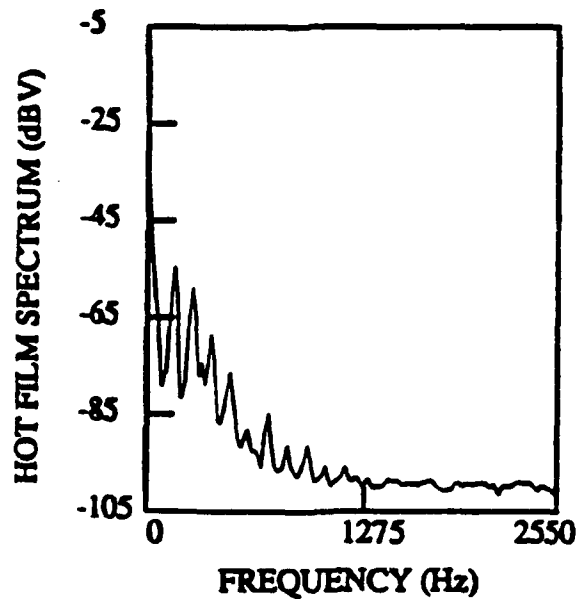
harmonic being seen than is expected based on the nominal range.) There is another reason for doing so in these experiments. The primary motion of the gas in this experiment is oscillatory and the hot film signal will be dominated by this oscillatory motion. The hot film sensing element cannot differentiate the direction of the velocity.: The output from the hot film, in the ideal case, will be a rectified velocity signal. This will be reflected in the spectrum as a strong peak at twice the frequency of the oscillation. The piston motion in this experiment, theoretically, consists of an infinite number of harmonics of the primary driving frequency and the hot film signal will also contain large numbers of harmonics. Due to the superposition of these harmonic motions, the rectified velocity signal appears to have its dominant frequency at the fundamental driving frequency rather than twice of that value as the case for a rectified pure sinusoidal oscillation. Therefore, the spectrum of such a signal will consist of infinite number of peaks at the driving frequency and its harmonics. One could be easily fooled by what appears to be a broad band spectrum if the spectrum examined is in the range of 0-2500 Hz (actually 0 to 2550 Hz). In this case the frequency resolution of the spectrum analyzer is much poorer, a point on the spectrum analyzer output may actually contain information of several harmonics of the driving oscillation. This is clearly illustrated in Figure 15, where spectral content of hot film output with piston running at 10 Hz is examined in both 0-100 Hz and 0-2500 Hz ranges. The spectrum in the 0-100 Hz range shows the velocity contains only the harmonic content of the driving oscillation and indicates a laminar flow, while the spectrum in 0-2500 Hz range appears to have a weak broad band appearance resulting from the poor frequency resolution. This could easily be mistaken as an indication of turbulence. The spectral content in the 0-2500 Hz range, however, can be used as an indication of the frequency extent of the broad band behavior.

Another approach is to study the actual hot film velocity signal. Perturbations on the main velocity signal are an indication of turbulence (Hino, et al. [21, 22]). Several disadvantages associated with the current experimental setup limit the effectiveness of this approach. First, it is difficult to differentiate the perturbations due to the higher harmonic motions of the fundamental driving oscillation and those random perturbations due to turbulence without some form of averaging. Second, when dry ice is used, one would expect to see oscillations not only in velocity but also in temperature, since a strong temperature gradient over the dry ice surface exists. The output of the hot film contains information due to both velocity and temperature variations. This problem cannot be solved with a temperature compensated probe, since the oscillation is at a high frequency and the phase between temperature and velocity variations is unknown. Certain information about the turbulence structure can still be obtained when such perturbations are large and cannot be explained by any harmonic components. It would be of interest to study the structure of turbulence using either a computer data collection system, where many samples can be collected and the variations analyzed, with a hot film anemometry or with a laser Doppler anemometry system. The latter approach is particularly of interest since it will diminish the influence of temperature variations.

In all the data presented below, the probe sensing element is perpendicular to the chamber floor. The output is mainly due to the acoustic velocity signal. One should keep in mind that the acoustic velocity amplitude at the sensor location may vary from case to case even at the same frequency as shown in Figure 16, where the



(a)



(b)

Figure 15
Hot film spectra with dry ice at the head end of the chamber, Infrared lamp off and piston running at 10 Hz: a) frequency range 0 to 102 Hz; b) frequency range 0 - 2550 Hz

estimated velocity amplitude at the probe location is plotted against the piston driving frequency for all four set ups. One should also avoid direct quantitative comparison between the cases of CDINL and HDINL and the cases of HFP and CFP, since the temperature at the sensor location also varies between cases with and without dry ice.

Figure 17 shows the spectra for driving at about 10 Hz for CFP, CDINL, HFP and HDINL cases. The spectrum frequency range is 0-100 Hz. Peaks are observed at the driving frequency (about 10 Hz) and all its harmonics. In some cases, the peak at 60 Hz is especially high, which is due to the superposition of the fifth harmonic of the piston motion and the electrical line noise. The spectrum for the CFP case is taken with piston running at about 11 Hz and the electrical line noise is seen at 60 Hz. In general, the spectra show the flows are laminar in all four cases since any turbulent component (represented by the spectral signal level between spikes) would be less than the background noise, if they exist. The only exception is the case of HFP, where the spectrum shows an excessive amount of noise at frequencies below 30 Hz. This phenomenon is very consistent, as will be shown in later figures, and indicates that the flow near the head end is: a) very sensitive to any initial disturbance; and/or 2) influenced by the large velocity gradient near the velocity node; and/or 3) influenced by the physical presence of the end plate; and/or 4) influenced by the wake caused by flow reversal over the hot film probe. This behavior was not obvious in the case of HDINL, which appears to confirm the stabilizing effect of the favorable thermal inversion.

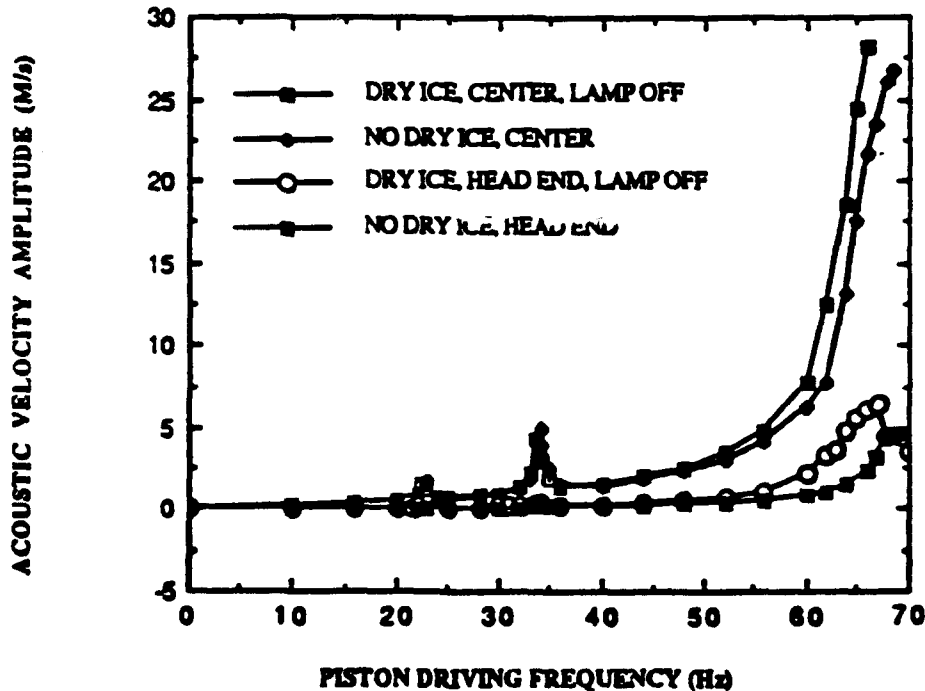


Figure 16
Oscillating velocity amplitude measured at the center of the dry ice versus piston frequency

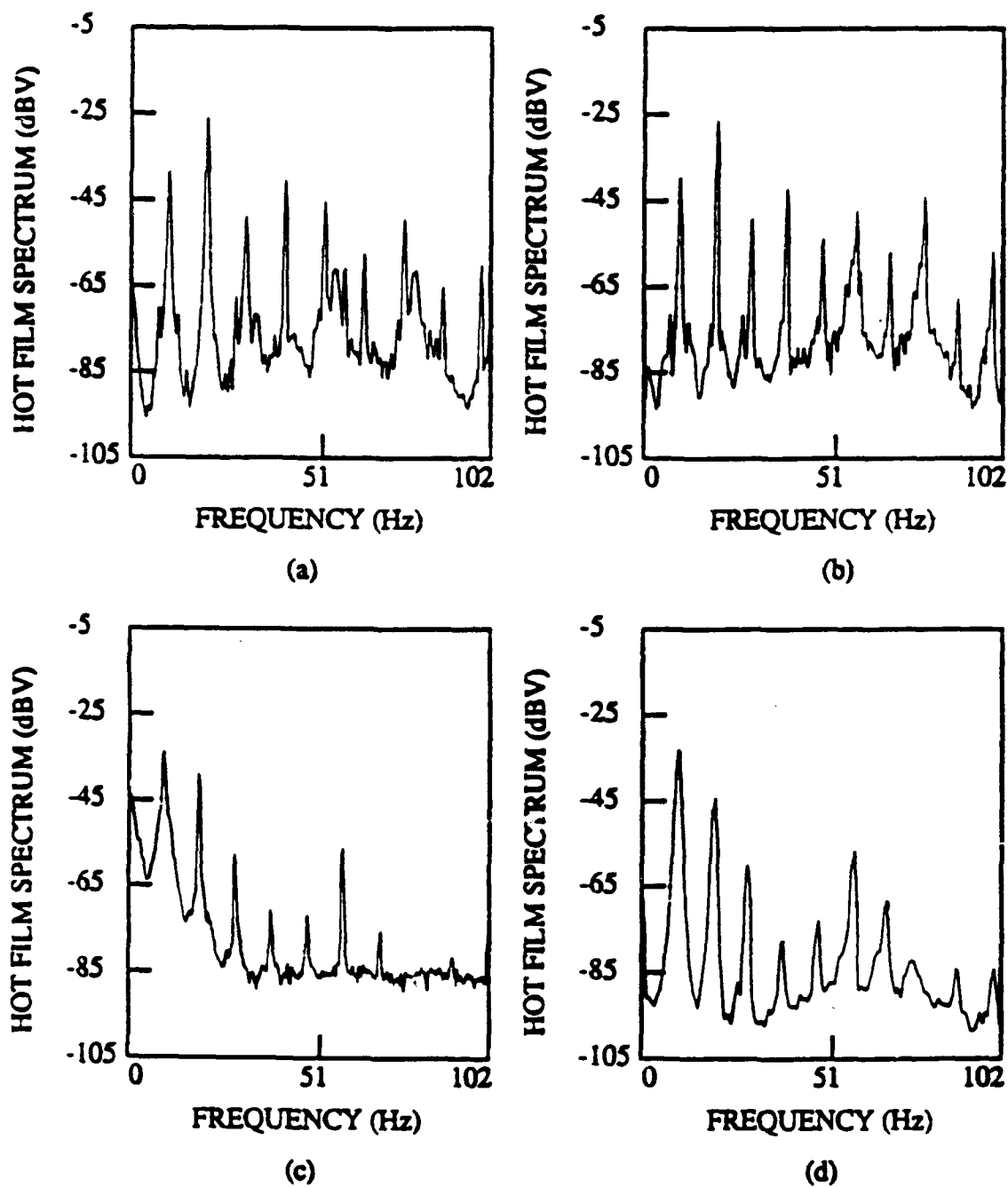


Figure 17
 Hot film spectra with the piston operating a 10 Hz for: a) probe at the tube center and no dry ice; b) probe and dry ice at the tube center with the IR lamp on; c) probe at the head end and no dry ice and d) probe and dry ice at the tube head end with the IR lamp on

Figure 18 shows the spectra of all four cases with driving at one third of the corresponding fundamental natural frequencies for the 0-100 Hz frequency range. The signal for the HFP case at low frequency is again observed to be the noisiest as indicated by the highest values of the background noise level which represents the turbulent component. The spectrum for HDINL case is the cleanest as it should be due to low acoustic oscillation amplitude. The spectra for the CDINL and CFP cases are slightly more turbulent looking than the HDINL case, probably due to higher velocity oscillation amplitudes in these two cases. These data appear to be in good agreement with the flow visualization where the flow in CDINL case exhibits some preturbulent instability at one third of resonance, while the flow in HDINL case is visually stationary and laminar.

Figure 19 contains the spectra for all four cases when the piston is running at one half of the fundamental natural frequency of each case. The spectra for CDINL, CFP and HFP are all broad band, although the acoustic velocity associated with the HFP case is much smaller than the others. It is believed that turbulent transition has occurred in those cases. The spectrum of the HDINL case indicates that the flow is still laminar. These results again support the findings of flow visualization, where the flow in the CDINL case is chaotic in nature while the flow in HDINL case barely exhibits a weak wave-like disturbance.

Figure 20 shows the hot film spectra at full resonance. The spectra show broad band behaviors for all four cases. Turbulence is believed to have occurred at full resonance for all cases.

A measure of the intensity of turbulence can be determined by examination of the spectrum in the frequency range of 0-2500 Hz. Figure 21 shows a series of spectra for the CDINL case at different driving frequencies on the 0-2500 Hz scale. It is obvious that when the flow becomes turbulent, the intensity of turbulence increases with increasing velocity amplitude as indicated by the increasing range of the broad band region. A rough estimate of turbulence intensity can be obtained by multiplying a characteristic turbulence signal level, which is taken to be the lowest value of the spectra between zero frequency and the piston frequency, and a cut-off frequency, at which the turbulence signal intensity level is 20 dBV (representing an order of magnitude smaller signal level) below the characteristic value. Figure 22 shows this approximate turbulence intensity, normalized to the value at resonance, as a function of the piston frequency for the cases without dry ice (Figure 22a) and the cases with dry ice (Figure 22b). It appears that the turbulence reaches its maximum for all cases at resonance, while local maximums also exist at one half of the resonant frequency.

Transition to turbulence can be determined by observing the spectrum of the hot film output while varying the piston driving frequency. When the spectrum first exhibits broad band appearance, transition to turbulence is said to have taken place. Figure 23 shows a series of spectra for the CDINL case at different driving frequencies. It can be observed that transition occurs at about 33 Hz, about 37 Hz (with turbulent flow between these frequencies) and again at about 50 Hz. The same procedure has been applied to HDINL case and the results are shown in Figure 24. Transition appears to occur at about 52 Hz. These findings again are in general agreement with the flow visualization.

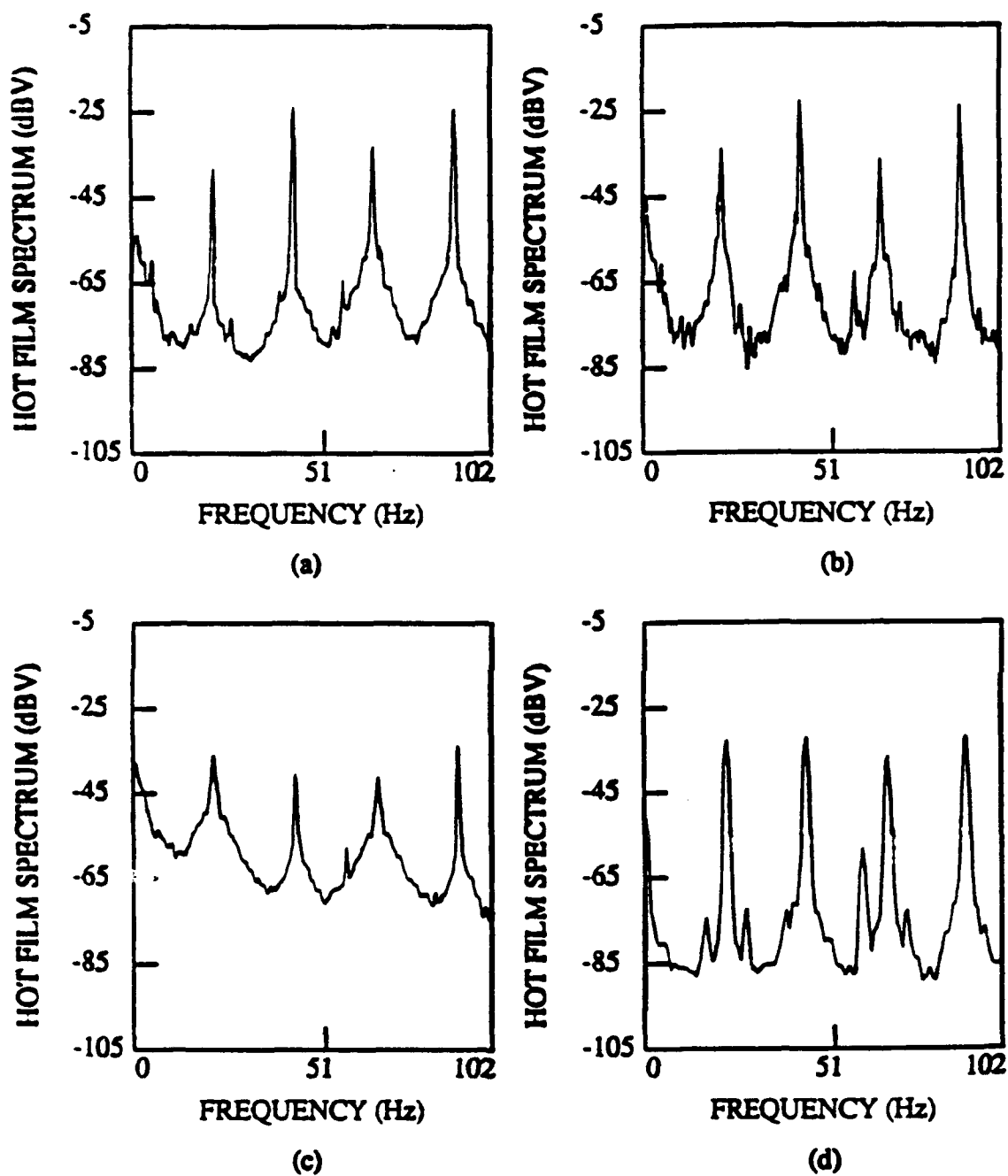


Figure 18
 Hot film spectra with the piston operating at one-third of the resonant frequency for: a) probe at the tube center and no dry ice; b) probe and dry ice at the tube center with the IR lamp on; c) probe at the head end and no dry ice and d) probe and dry ice at the tube head end with the IR lamp on

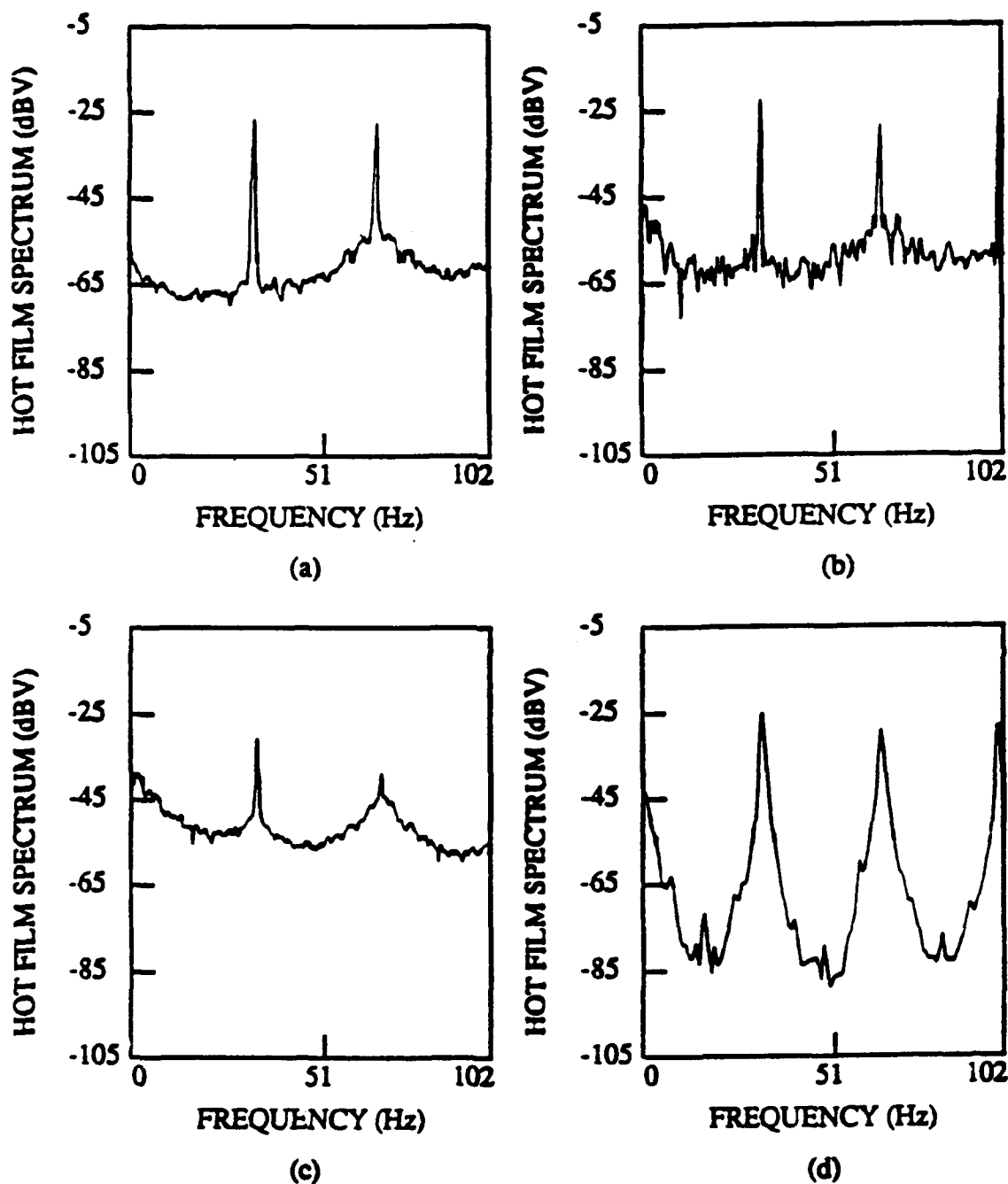


Figure 19

Hot film spectra with the piston operating at one-half of the resonant frequency for: a) probe at the tube center and no dry ice; b) probe and dry ice at the tube center with the IR lamp on; c) probe at the head end and no dry ice and d) probe and dry ice at the tube head end with the IR lamp on

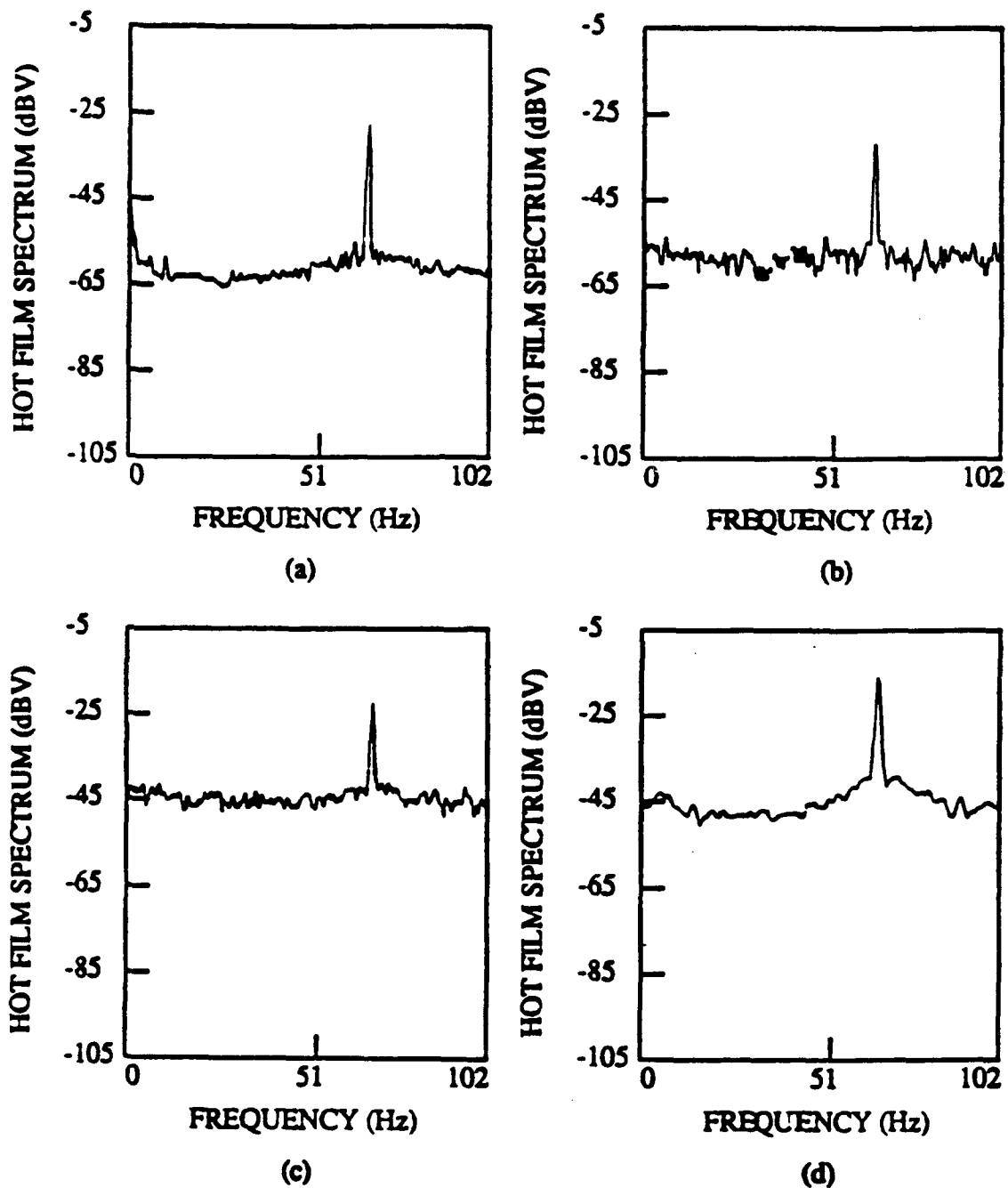


Figure 20
 Hot film spectra with the piston operating at the resonant frequency for:
 a) probe at the tube center and no dry ice; b) probe and dry ice at the
 tube center with the IR lamp on; c) probe at the head end and no dry ice
 and d) probe and dry ice at the tube head end with the IR lamp on

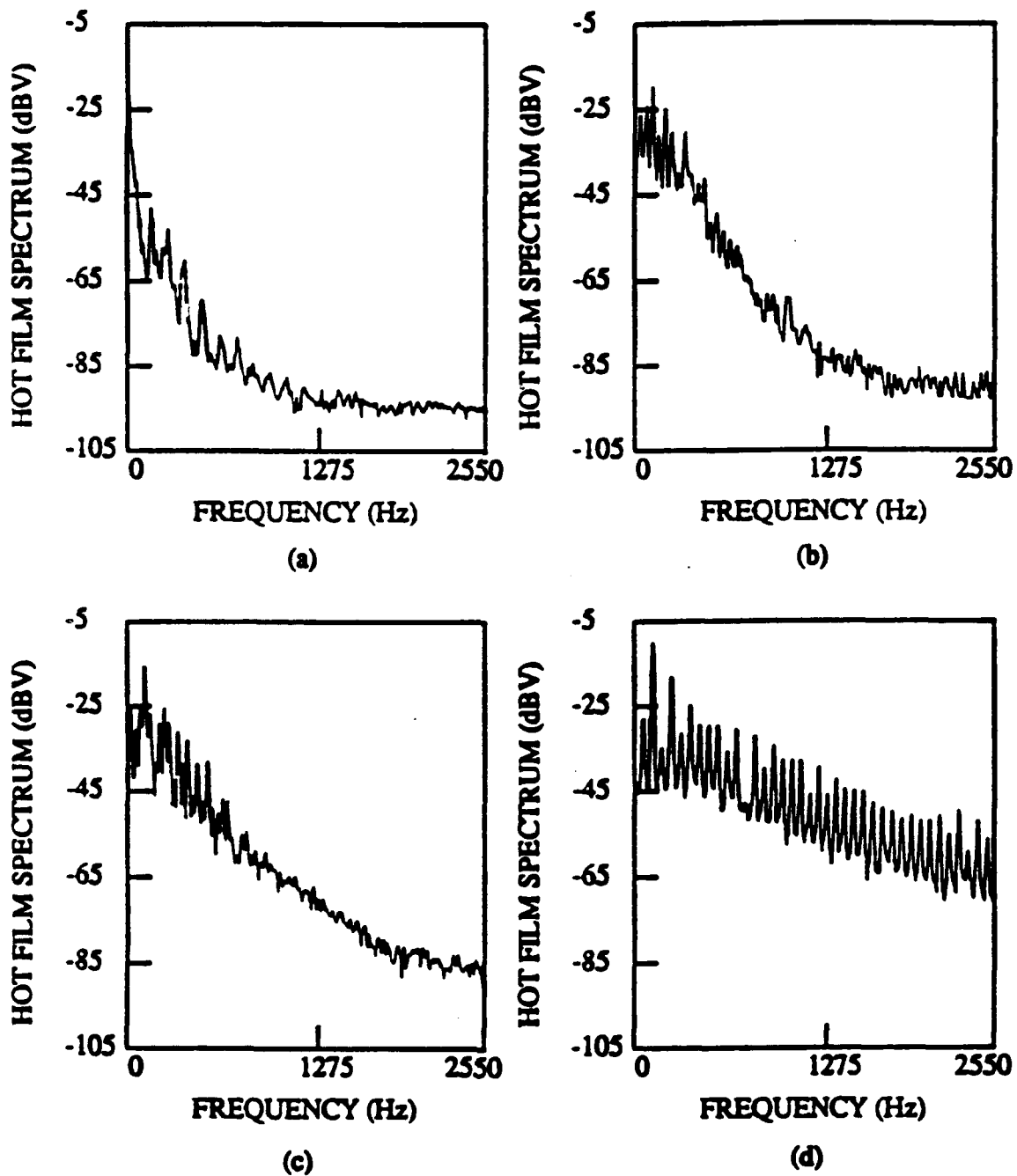
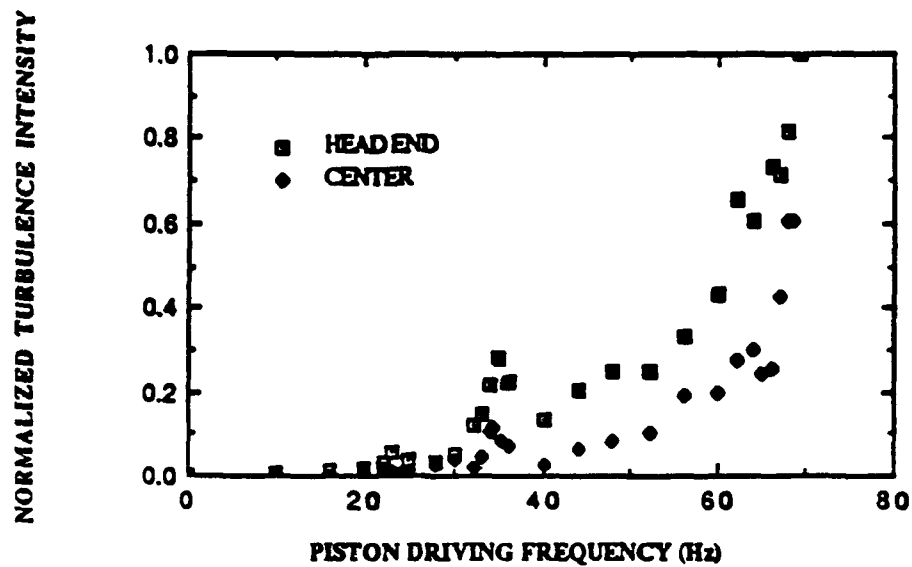
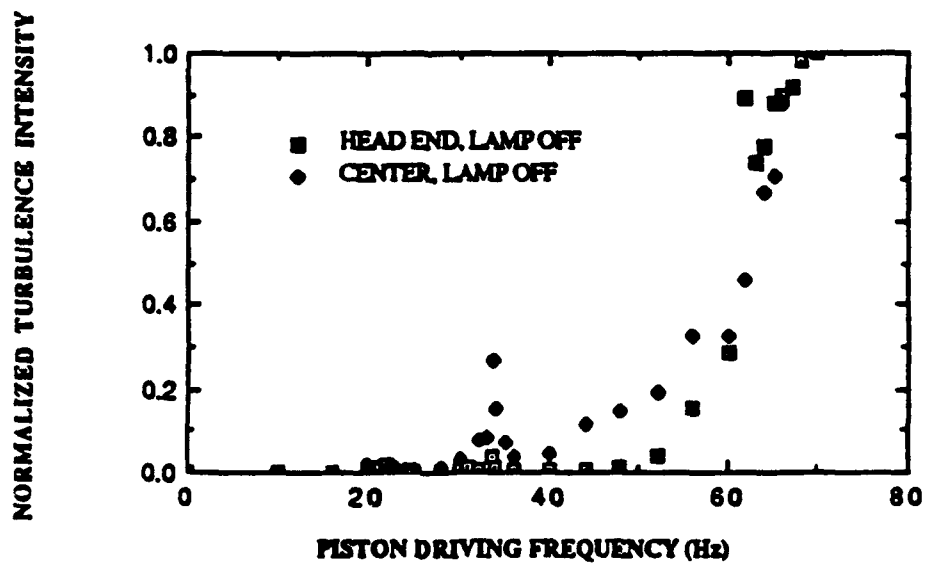


Figure 21
Hot film spectra with the piston operating at different frequencies
with the dry ice at the chamber center and the IR lamp off: a) 10
Hz; b) 22.4 Hz; c) 33.7 Hz and d) 66 Hz

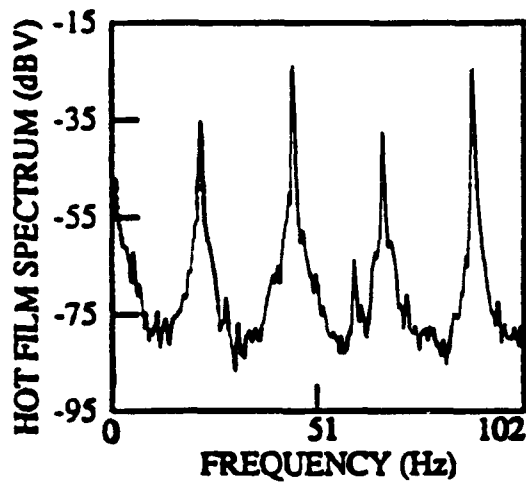


a)

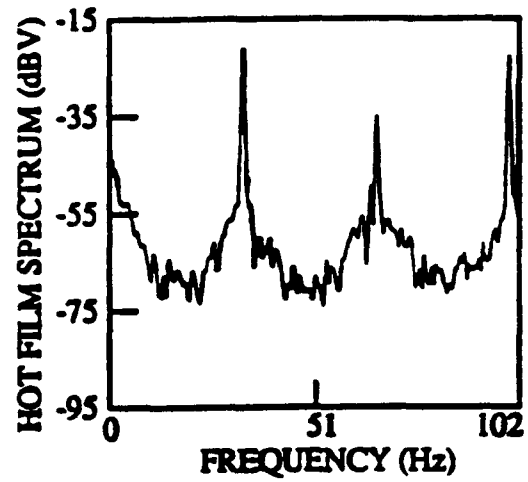


b)

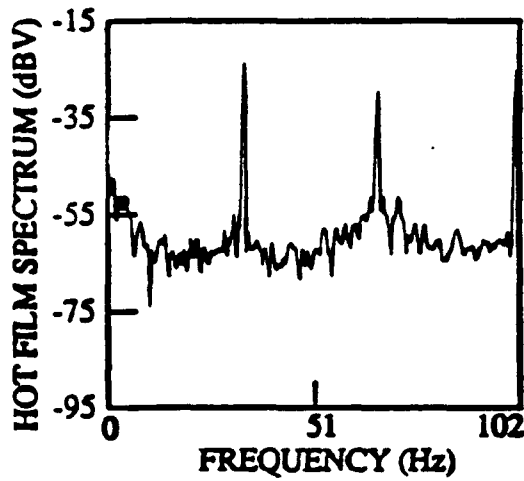
Figure 22
 Normalized approximate turbulence intensity versus piston frequency: a) no dry ice and b) with dry ice



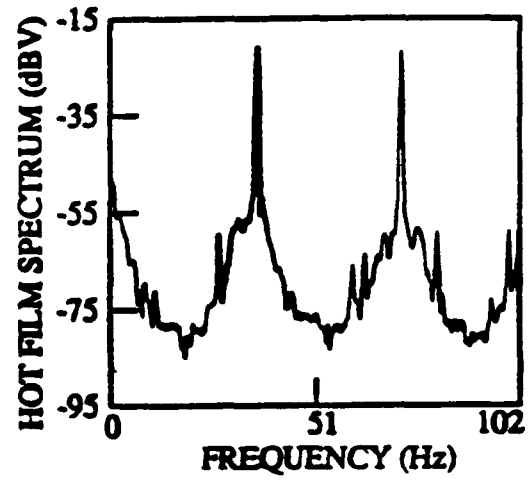
(a)



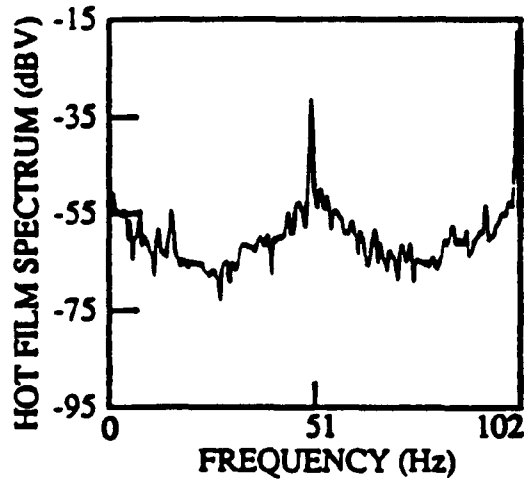
(b)



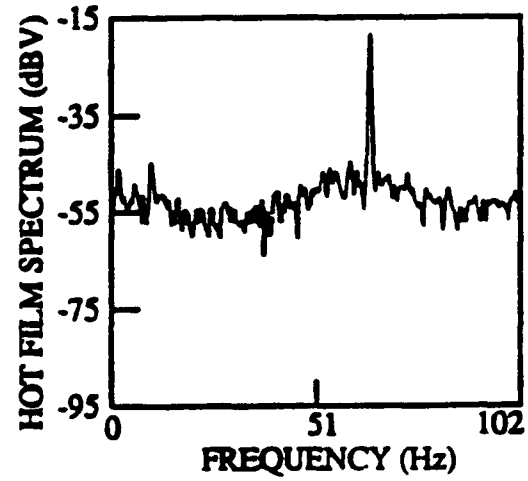
(c)



(d)



(e)



(f)

Figure 23

Hot film spectra for the case of the dry ice at the chamber center and the lamp off, at piston frequencies of: a) 22.4 Hz; b) 33 Hz; c) 34.2 Hz; d) 36 Hz; e) 50 Hz and f) 64 Hz

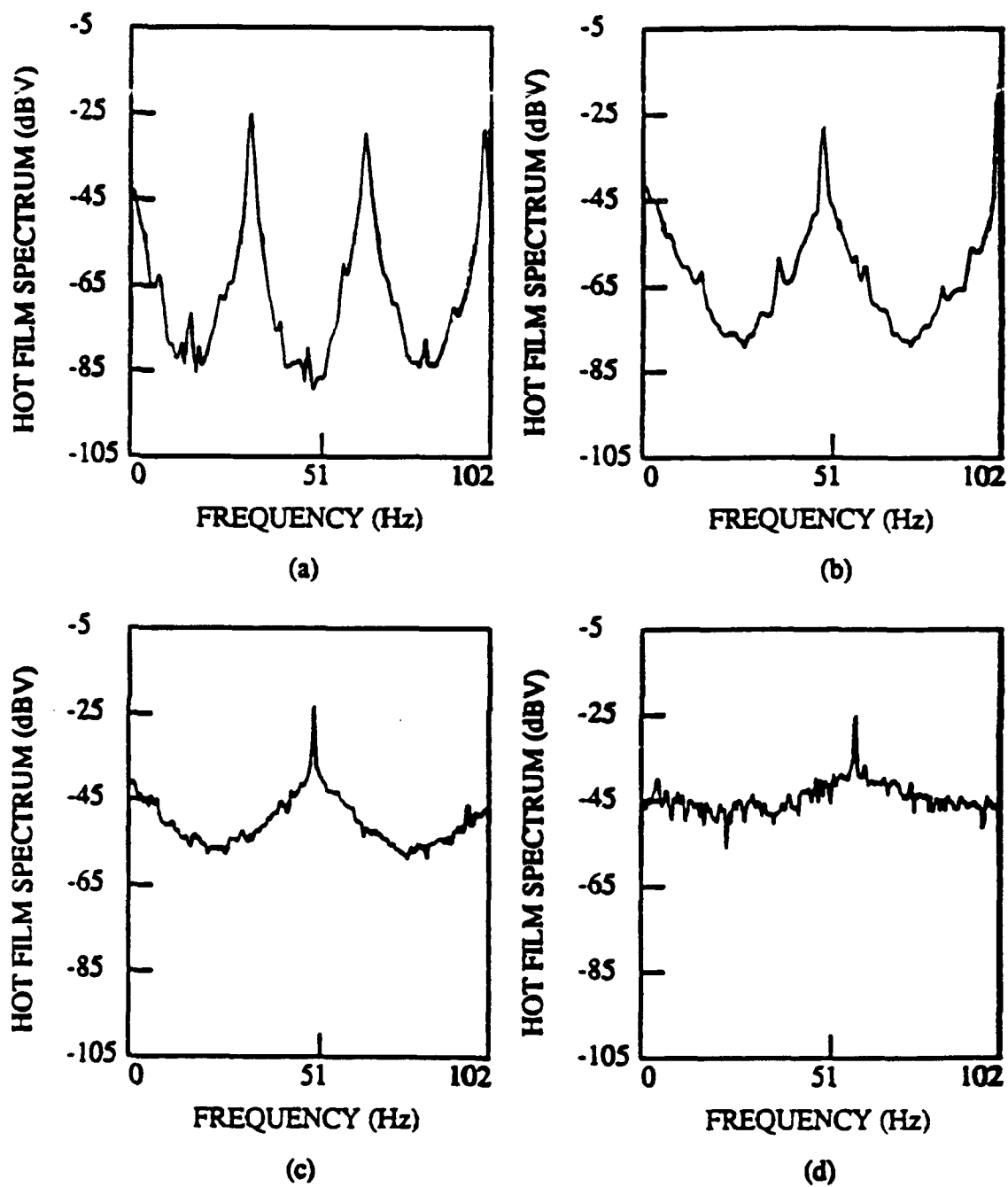


Figure 24
 Hot film spectra for the case of the dry ice at the head end of the chamber and the lamp off, at piston frequencies of: a) 33 Hz; b) 50 Hz; c) 52 Hz and d) 60 Hz

The transition determined this way is believed to determine the critical point at which the weakly turbulent flow (category 2 as discussed in the introduction section) occurs. Observation based on spectral output of hot film cannot distinguish the difference between weakly turbulent flow, conditional turbulent flow or fully turbulent flow because the spectrum is averaged over several oscillation cycles. Examination of the actual hot film signal is required in order to find the fine details of the turbulence.

Figure 25 shows a set of hot film signal traces for the CDINL case. The signal at one third of the fundamental natural frequency is the superposition of the main driving oscillation and the first acoustic mode of the chamber, otherwise the signal is fairly smooth. The signal at one half of the natural frequency starts to show a growing small amplitude, high frequency perturbation over the main signal, possibly indicating a weakly turbulent flow. There are some indications of possible steepening of the wave front although the pressure signal in this case does not have any shock-like appearance. The pressure signal is free of any possible influences from the flow environment, it is believed that the weak indication of a shock is either a result of the previous discussed limitations on hot film measurement associated with this study or a distortion of the wave form due to turbulence (Hino, et al.[21,22]). Comparison of the traces shows that the more violent type of turbulence or conditional turbulent flow as categorized by Hino and his coworkers occurs at about 64 Hz. Occurrence of a shock is obvious, based on both velocity and pressure signals in this case.

As a further comparison, the transition into conditional turbulence over the nontranspiring surface is illustrated in Figure 26, where several hot film traces for CFP case are presented. In this case, transition appears to occur at 65 Hz, corresponding to an acoustic Reynolds number Re_a of 820, comparable with the values obtained by previous researchers. The difference between the acoustic Reynolds number in this case and the previous work could possibly be due to flow reversal over the probe and surface roughness, both of which could contribute to early transition. The same approaches yield a critical Reynolds number Re_a of only about 70 for the HFP case. This wide variation in transition value again indicates the possible difference in the mechanisms that trigger turbulence at velocity node and antinode. In all cases, bursting type of turbulence is seen to occur only after a shock has been developed in the acoustic field.

The most interesting phenomenon in the turbulence structure in Figures 25 and 26 is that the turbulence appears to not persist over the whole cycle of oscillation, which also occurs in the nontranspiring surface case. This cyclic laminar-turbulent behavior may have a profound influence in the heat transfer mechanism associated with this type of flow as will be discussed in the next section.

Mass Flow and Heat Transfer Results. Figure 27 shows the measured mean volume flow rate versus the driving frequency of the piston for the four cases with dry ice in the chamber. In the cases of no acoustic oscillation, the steady state mean flow rates are the same for the CDILO and HDILO cases. The flow rates are lower but also the same for the CDINL and HDINL cases. The difference between the two sets is caused by the infrared radiation applied in the CDILO and HDILO cases and the absence of the radiation in the CDINL and HDINL cases. At low piston driving frequencies, no increase in the mean flow rate has been observed in any case. An

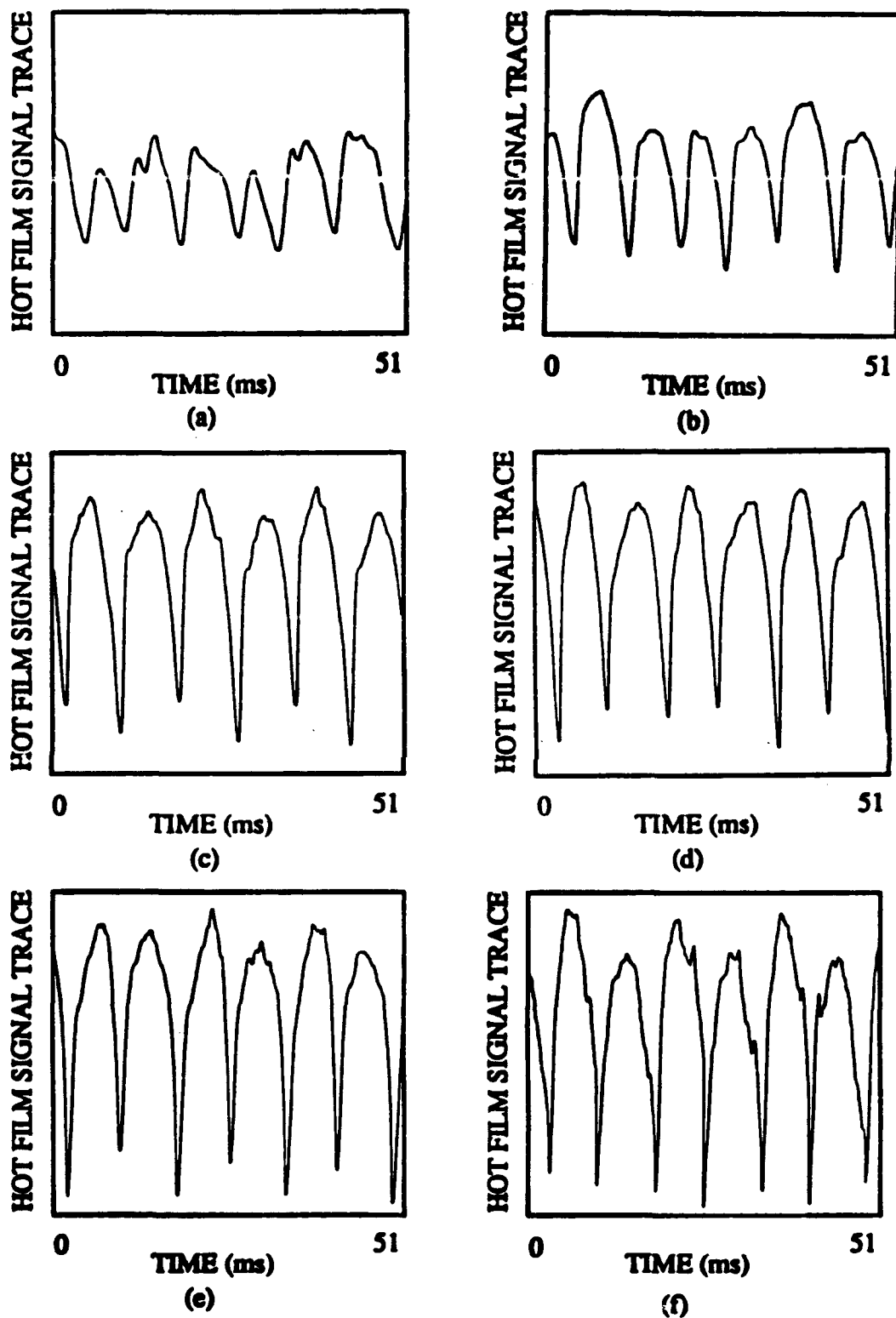


Figure 25
Hot film spectra for the case of the dry ice at the chamber center and the lamp off, at piston frequencies of: a) 22.4 Hz; b) 34.2 Hz; c) 60 Hz; d) 63 Hz; e) 64 Hz and f) 66 Hz

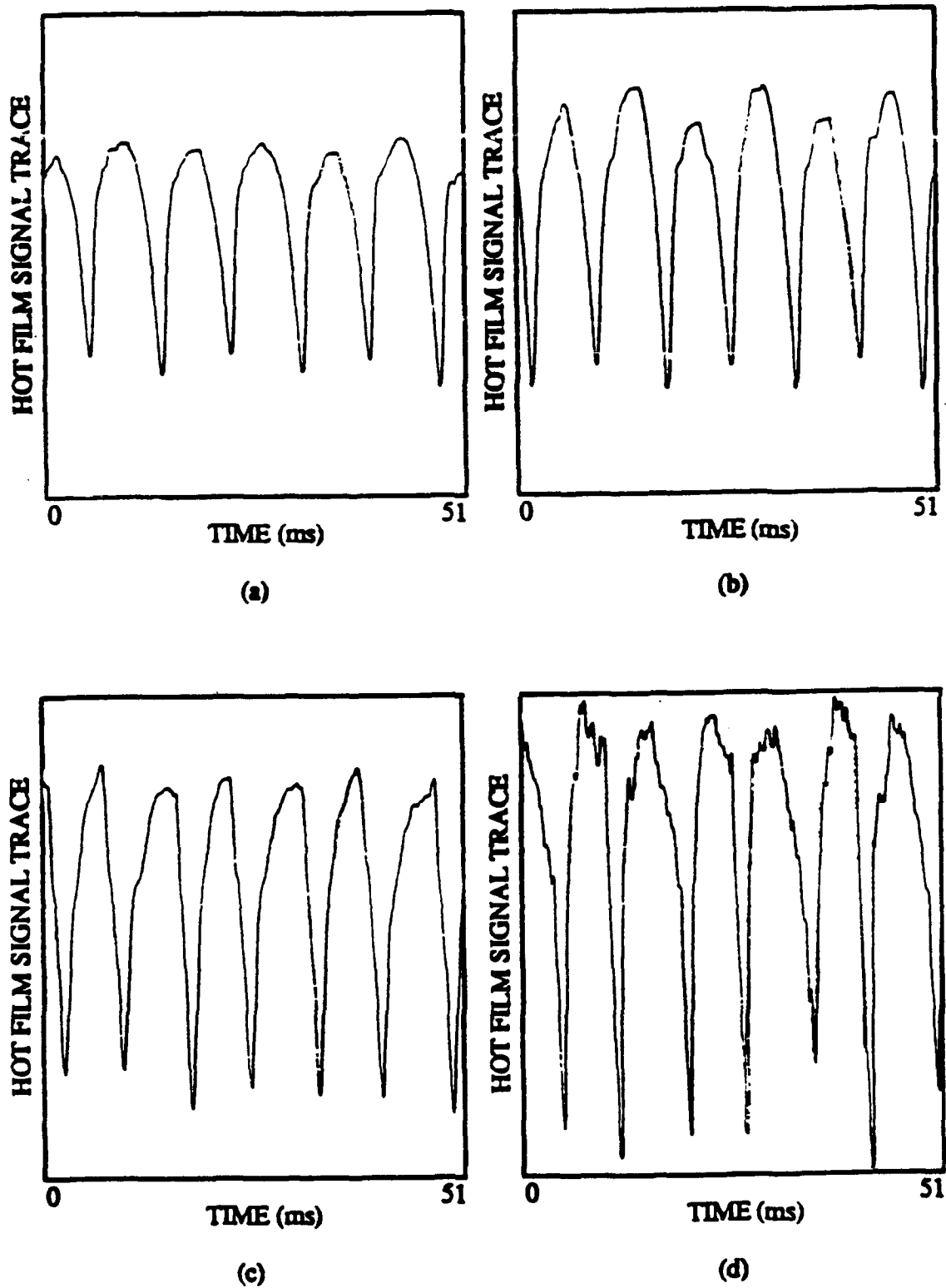


Figure 26
 Hot film spectra for the case with no dry ice, at piston frequencies of: a) 60 Hz; b) 64 Hz; c) 65 Hz and d) 67.2 Hz

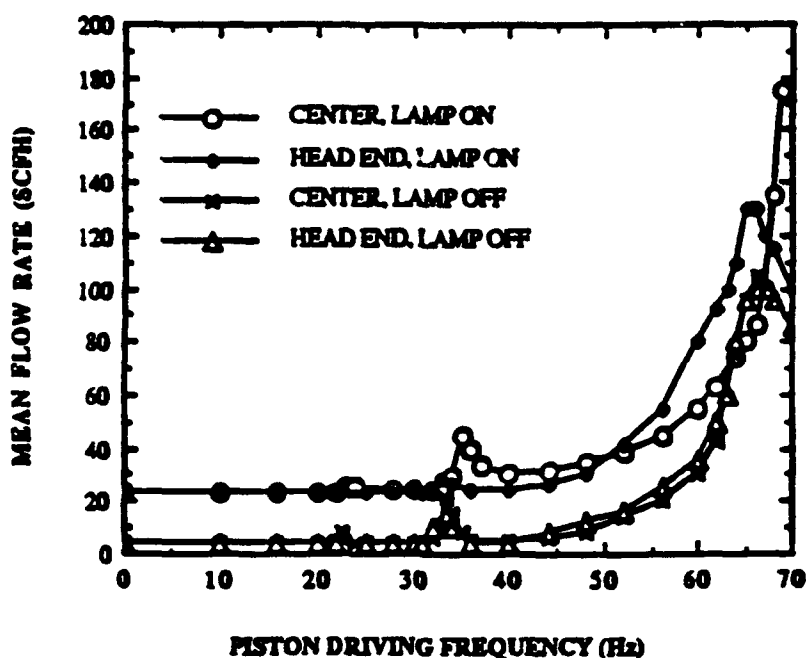


Figure 27
Mean flow rate versus piston frequency

increase in the flow rate has been recorded when the piston speed is one third of the fundamental natural frequencies of the chamber in the CDILO and CDINL cases. Increase in the dry ice sublimation rate has also been observed near one half of the natural frequencies for all four cases. The magnitude of the increase in the sublimation rate is always higher when the dry ice is located near the center of the chamber. A dramatic increase in the flow rate has been measured when the piston frequency is near any of the fundamental natural frequencies. Again the maximum flow rates measured are higher when the dry ice is located near the center. The nearly horizontal line on Figure 27 is a calculated value of the flow rate versus frequency based on the thermodynamic property of the dry ice and the measured change in the mean chamber pressure for the cases with infrared radiation. The increase in mean pressure clearly does not explain the major increases in the sublimation rate that are observed.

A comparison of Figures 8 and 27 indicates that an increase in the dry ice sublimation rate accompanies the increase in the acoustic oscillation amplitude. As discussed previously, an increase in the acoustic pressure will cause an increase in the sublimation rate since the heat of sublimation decreases with increasing pressure. The mean sublimation rate over an oscillation cycle should not change with this type of simple linear coupling mechanism. A possible nonlinear pressure coupling could cause an increase in the mean sublimation rate with increasing pressure amplitude, but one would expect to see a smaller increase in the mean sublimation rate when the dry ice is located near the center of the chamber, the pressure node. The inability to

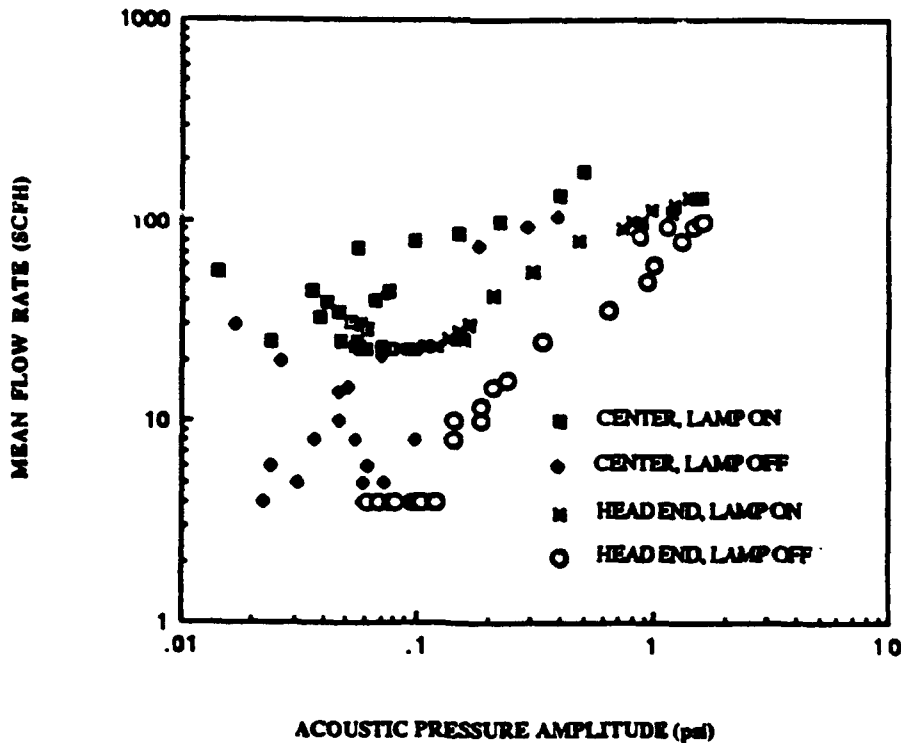


Figure 28
Mean flow rate versus the amplitude of the oscillating pressure

explain the mean flow rate increase due to pressure is supported by the curves in Figure 28 where the mean sublimation rate is plotted against the acoustic pressure amplitude at the center of the dry ice. No clear direct dependence of sublimation rate on acoustic pressure amplitude is observed, particularly when the dry ice is located near the center. The increase in the mean sublimation rate is not due to the change in the heat of sublimation of the dry ice as a result of pressure change, but rather is due to a change in the heat transfer mechanisms which are associated with the oscillatory motion of gas parallel to the dry ice surface. Heat transfer and the resulting mass flow rates would be expected to be very strongly effected by whether the flow is laminar or turbulent. Discussions in previous sections have shown that turbulence did indeed occur in this experiment and its occurrence has also been seen to cause the increase in the mean sublimation rate. The transition to turbulence and the turbulence intensity are largely determined by the Reynolds number, in this case the acoustic Reynolds number and it is reasonable to suggest a dependence of the sublimation rate on the acoustic velocity or acoustic Reynolds number. The observed large increase in the sublimation rate with dry ice near the center of the chamber also indicates this kind of dependence, since a velocity antinode is located at the chamber center.

Figure 29 shows the mean sublimation rate as a function of the acoustic Reynolds number. The results show a clear dependence of sublimation rate on the acoustic Reynolds number that is physically reasonable. The lines have been added to clearly group the four sets of data.

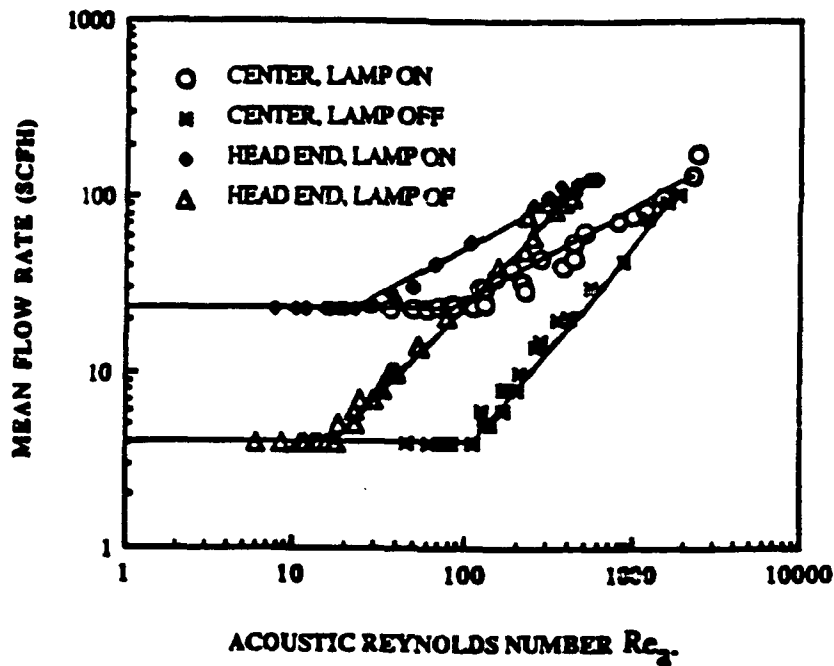


Figure 29
Mean flow rate versus the acoustic Reynolds number

In the cases of no infrared radiation (e.g., CDINL and HDINL), the sublimation of dry ice is dominated by the combination of natural convection and conduction effects at low acoustic excitation cases. The flow above the subliming dry ice surface is laminar. As the acoustic velocity amplitude increases, the flow above the dry ice surface becomes unstable. Transition to turbulence occurs as the acoustic Reynolds number reaches a critical value, which is indicated in the sharp increase in the sublimation rate. In this case the heat transfer mechanism is dominated by forced turbulent convection. The turbulence intensity has been shown to increase with increasing acoustic disturbance and the sublimation rate, also, increases with increasing acoustic oscillation amplitude.

In the cases where infrared radiation is applied over the dry ice surface, the radiation heat transfer mechanism initially dominates the weak natural convection and conduction effects in the laminar case, and a higher steady state sublimation rate is measured at low acoustic amplitude. As the acoustic disturbance increases in amplitude, the boundary layer again becomes unstable. A higher transition acoustic Reynolds number is observed for the HDILO case while a lower transition acoustic Reynolds number is observed for the CDILO case as compared with their counterparts without infrared radiation. As the flow becomes more unstable, increases in the sublimation rate are observed as the turbulent convection increases the heat transfer to the dry ice surface. When the flow over the dry ice surface becomes turbulent, the optical thickness of the CO₂ gas above the dry ice increases due to an increased sublimation rate and turbulent mixing. The heat received by the surface through radiation thus decreases. This results in a more gradual increase in the mean sublimation rate as compared to the sharp increase in the cases without external

radiation. As the turbulence intensity increases, the sublimation rate of the dry ice increases, but so does the effective optical thickness of the CO₂ gas. The effect of turbulent convection becomes more dominant while the effect of radiation diminishes. The curves for the cases with and without infrared radiation appear to merge into each other as the turbulent convection heat transfer mechanism controls the sublimation process of the dry ice.

The threshold values of acoustic velocity amplitude at which the dry ice sublimation rate starts to increase are about a factor of two less in the cases with dry ice located at head end than at the center, indicating possible difference in the triggering mechanisms for the turbulence to occur as observed by flow visualization and hot film anemometry.

Another point needed to be addressed is the similarity in the slopes of the curves in Figure 29. The slopes of curves for CDILO and HDILO are very similar, and also the slopes of curves for CDINL and HDINL. This again supports the suggested heat transfer mechanisms. A universal curve can be generated for this experiment by plotting the increased mean flow rate as a function of a ratio of an excess acoustic Reynolds number to the threshold value as shown in Figure 30, where $Re_{a\ ini}$ is the acoustic Reynolds number at which initial increase in the dry ice sublimation rate is observed. The data points for all four different experimental cases collapses on to a single curve strongly supporting the dominance of the turbulent forced convection heat transfer mechanism in the experiments. The scattering of data at low increased sublimation rate is due to the occurrence of preturbulence instability. The increased sublimation rate is proportional to the increased heat transfer rate due to turbulent forced convection. This curve actually indicates a dependence of the turbulent heat transfer rate in oscillatory fluid to the amplitude of the oscillation. Curve fitting all the data yields a relation of the form

$$h \propto \left(\frac{Re_a}{Re_{a\ ini}} - 1 \right)^{0.8124} \quad (11)$$

where 0.8124 is the slope of the curve on the log-log plot and h is turbulent convective heat transfer coefficient. If the points representing the preturbulent instability as observed with flow visualization are removed, curve fitting the data then yields a relation of the form

$$h \propto \left(\frac{Re_a}{Re_{a\ ini}} - 1 \right)^{0.7937} \quad (12)$$

From these results it is reasonable to suggest an empirical relationship of the form

$$h \propto \left(\frac{Re_a}{Re_{aini}} - 1 \right)^{0.8} \quad (13)$$

This empirical relationship is very important since it provides a means of predicting the response of a subliming surface to acoustic oscillation in velocity coupling. Moreover, this correlation bears a striking similarity to the widely accepted convective heat transfer correlation for fully turbulent nonoscillatory flow, where convection heat transfer coefficient is expressed as

$$h \propto Re^{0.8} Pr^{\frac{1}{3}} \quad (14)$$

where Re is the mean flow Reynolds number and Pr is the Prandtl number. This similarity again supports the occurrence of turbulence in the experiments. The dependence on Prandtl number has not been obtained since Prandtl number is nearly constant for all cases in this study. The ratio of Reynolds numbers in the correlation for oscillatory flow is determined by the nature of the turbulence in oscillatory flow. Turbulence appears to occur only when Reynolds number is sufficiently high and persists during part of the oscillation cycle, the ratio $(Re_a - Re_{aini})/Re_{aini}$ provides a measure of the percentage of the flow being turbulent during a cycle as well as the intensity of the turbulence.

Comparison with actual rocket propellant results of Crump and Price [6] and of Medvedev and Revyagin [11] is possible by dividing the increased mean sublimation rate with the corresponding steady state sublimation. The slopes of the data will not be affected by this operation when presented in log-log form. The resulting value is the same as the increased regression rate which is used by previous researchers in presenting their data. Although the data presented by the previous researchers are given in terms of an acoustic velocity amplitude, the ratio of increased Reynolds number $(Re_a - Re_{aini})/Re_{aini}$ is the same as the ratio of acoustic velocity amplitude $(U - U_{ini}) / U_{ini}$ provided that the frequency of the oscillation and the viscosity are constant throughout their experiment, where U_{ini} is the acoustic velocity amplitude corresponding to Re_{aini} . The information provided by Crump and Price shows that it is true in their experiments, while it is assumed to be true for the Medvedev and Revyagin experiments due to lack of further information. A striking similarity in the slopes of all experiments is observed and shown in Figure 31. This suggests that the same mechanism (occurrence of turbulence or turbulent forced heat convection) is responsible for the increase of the mean burning rate of propellant in these previous experiments. The reason that all these curves do not fall into one curve here is the differences in the steady state heat transfer mechanisms. The empirical relationship developed above appears to hold for all cases, i.e.,

$$\frac{r_a}{r_{st}} - 1 \propto \left(\frac{Re_a}{Re_{aini}} - 1 \right)^{0.8} \quad (15)$$

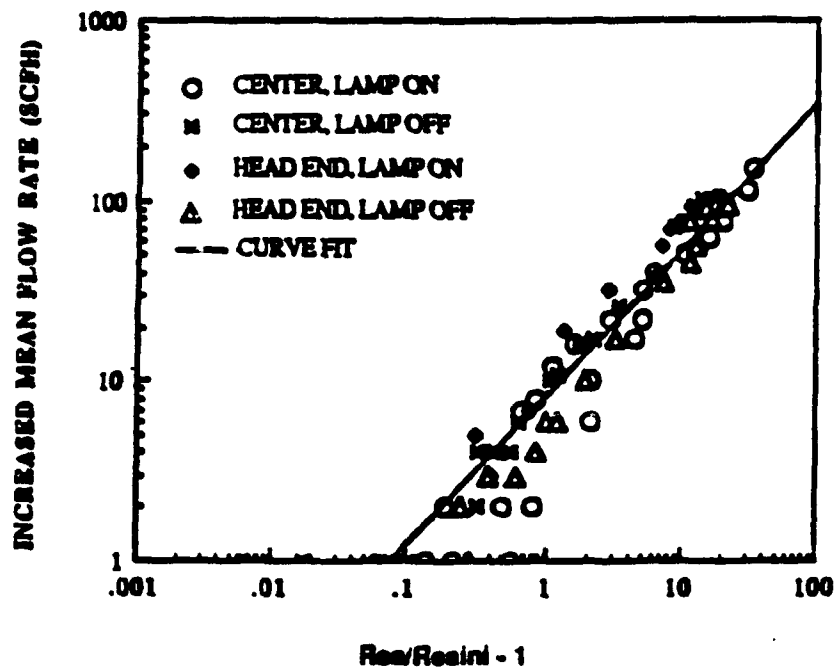


Figure 30
Increase in mean flow rate (beyond the case with no oscillations) versus the fractional increase in the acoustic Reynolds number (above the transition value)

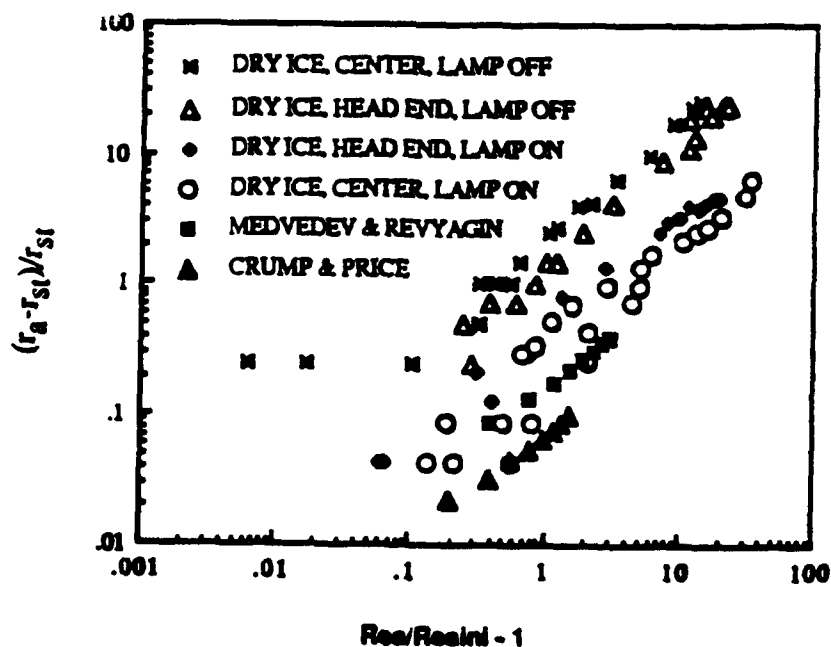


Figure 31
Fractional increase in the surface regression rate (beyond the case with no oscillations) versus the fractional increase in the acoustic Reynolds number

where r_{st} and r_a are the steady state surface regression rate and the surface regression rate due to acoustic disturbance.

A nonlinear effect such as thermal-acoustic heating [28] is very unlikely to be responsible for the increase in sublimation rate. This mechanism increases with the strength of the shock wave and the shock is very weak near the chamber center even at resonance. This effect has been observed to act like a heat pump; it cools the boundary at velocity antinode while it transfers energy to the pressure antinode. Acoustic streaming, on the other hand, may contribute to the increase in the mass flow rate, since it results in a mean circulation of flow from velocity antinode to pressure antinode along the surface, which in turn can trigger a steady state erosive type of phenomenon. The distribution of the streaming velocity is very similar to that of a second velocity mode, and it should be expected that the effect of acoustic streaming is similar in all the cases with dry ice, since the relative location of the dry ice and the velocity antinode is almost identical to the relative location of head end dry ice to pressure antinode. It is also not clear how a second order effect such as acoustic streaming may feed energy into first order acoustic wave motion based on the classic acoustic streaming theory.

The implications of the discussions in previous sections can be summarized as:

1. Energy in the acoustic waves has been increased as a result of the increasing sublimation of the dry ice (simulated increased burning rate of the solid propellant).
2. Heat is also transferred back to the simulated propellant surface due to an acoustic wave induced mechanism.
3. The responsible coupling mechanism is related to the acoustic velocity oscillation and the occurrence of turbulence.

Transition Reynolds Numbers. It should be clear by now that the determination of transition to turbulence is very important since it will eventually enable prediction of the response of the combustion process to velocity oscillation parallel to the propellant surface. A comparison with the theoretical results of Beddini and Roberts is shown in Figure 32, where U , V , f , and ν are the local acoustic velocity, injection velocity, piston driving frequency and kinematic viscosity, respectively. The solid curve is the prediction of Beddini and Roberts for isothermal flow over a smooth surface. They predict turbulent flow for conditions above the curve and laminar below the curve. The experimentally determined transition regions are presented in several groups. The initial occurrence of turbulence (or weakly turbulent flow) has been determined by means of a) flow visualization; b) observing hot film spectrum; and c) flow rate measurement. These results agree fairly well with each other, particularly, for the cases where dry ice is located near the center. The transition to bursting type of turbulence (or conditional turbulent flow) is determined by analysis of hot film traces.

It is seen that when the dry ice is located near the center, the critical Reynolds number for transition to weakly turbulent flow is about a factor of 2.5 lower than the theory predicts for a smooth surface and isothermal flow. The critical Reynolds number for transition to conditional turbulent flow or bursting type of turbulent flow is a factor of two lower than the theoretical prediction. The theory does not differentiate the types of turbulence that are possible to occur in an oscillatory flow, it appears that their prediction applies to the occurrence of weakly turbulent flow condition. The discrepancy between the experiments and the theory in predicting the transition to weakly turbulent flow may occur due to several reasons. First, the theoretical prediction is based on the conditions that the wall is perfectly smooth, has a uniform injection and no initial turbulence exists. In this experiment the dry ice surface has a finite surface roughness, the surface injection rate is not perfectly uniform and the amount of initial turbulence is unknown. Any of these factors may cause early transition to turbulence. Second, an isothermal condition has been assumed by Beddini and Roberts, while in our experiment a strong temperature gradient exists near the dry ice surface. No other theoretical results are presently available. The experimental results seem to agree fairly well with the previous work conducted over

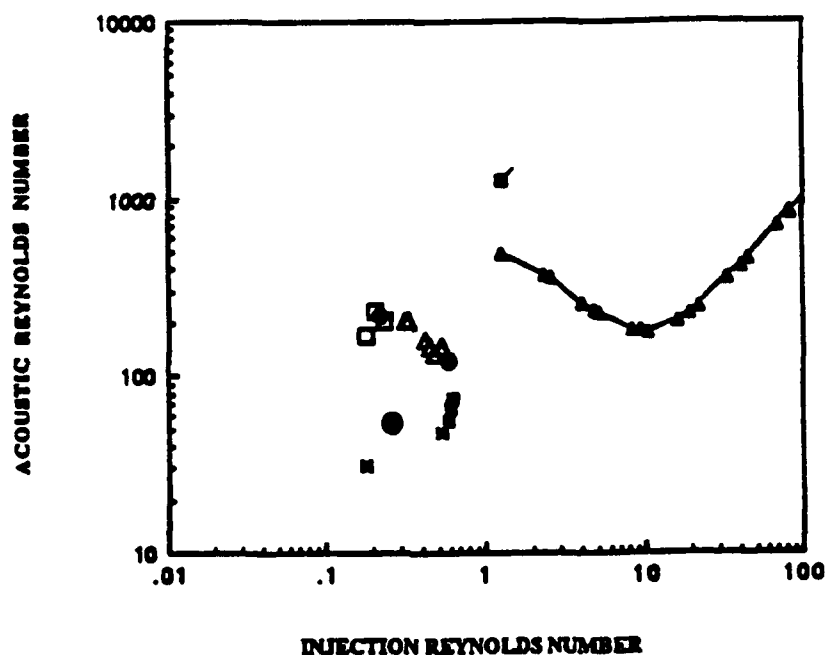


Figure 32.

Effect of surface injection on the transition to turbulence. All are experimental values with dry ice with one exception: \square at the center based on hot film results; \triangle at the center based on flow visualization; \bullet at the center based on mean flow rate; \circ at the head end based on hot film results; \blacksquare at the head end based on flow visualization; \blacksquare at the head end based on mean flow rate; \blacksquare at the head end based on hot film results for bursting type of turbulence; \blacktriangle numerical predictions of Beddini and Roberts [12]

nontranspiring surfaces. The transition at the head end is considerably lower than the theory predicts. As has been discussed extensively in previous sections, further study is necessary to understand the different behavior of the flow in this case as to the transition near the pressure node.

Laser Doppler Flow Field Measurements

Laser Doppler Anemometer Results. Considerable effort has been expended to obtain quantitative flow field measurements with a laser Doppler anemometry system. Dantec Inc. designed the two velocity component system to be used for either steady or periodic flows. The data collection is carried out in two stages. Dantec supplied hardware carries out the signal conditioning, filtering, timing and analog-to-digital conversion. A personal computer using Dantec supplied software carries out the final data analysis, data presentation and overall control of the system. Two versions of this software exist; one for steady flow measurements and a second for periodic flows. The periodic flow software was used during most of this project. This software was designed to produce a phase averaged result.

A simple optical trigger and synchronizing disk attached to the crankshaft of the piston generated the timing signal needed for the phase averaging. This trigger system produced one trigger signal per cycle of the piston. The period between two successive timing signals is a cycle and corresponds to a 360° rotation. The 360° between trigger signals is divided into a series of "bins" each with some angular width and together making up the total 360° . (For example, if the bin width is chosen to be 10° there are 36 bins.) Every datum collected falls into a bin. When sufficient data have been collected, the contents of each bin can be statistically analyzed to learn the characteristics of the flow at that particular phase in the cycle. This type of approach is necessary when such a small number of data are obtained during a single cycle of the periodic flow that the data from only one cycle does not yield a realistic picture of the flow during that cycle. Using dry ice, with no additional particles added, the data rate was approximately 100 Hz, the resonance of the dry ice chamber was about 60 Hz, and only about two data were obtained in a typical cycle. Two measurements during a cycle will clearly not yield a clear picture of the velocities during the cycle and phase averaging is necessary. If a time series for the data was available it could yield a good description of the periodic flow at frequencies less than 10 Hz, but these low frequencies are not of particular interest. The Dantec periodic flow software does not supply the data time series.

Attempts to use this approach to measure the periodic flow have consistently failed to produce a meaningful and plausible result. This failure appears to be due to either extremely low velocities; unknown problems within the software system; the very limited region above the dry ice where the particles are moving with the gas flow or a combination of these.

As noted earlier the sublimation rate of the dry ice will give a velocity normal to the dry ice surface of approximately one centimeter per second. This velocity is at the lower limit of detectability of the LDA system. If the system is operated in the steady

flow mode above the dry ice mean velocities of this magnitude are detected. The velocity distribution, in this case, shows no clear peak. This may be due to a very wide velocity distribution of particles from the dry ice or very significant amounts of noise. When the system is driven by the piston, velocities will vary from zero to perhaps a few centimeters per second and be more difficult to detect.

When the system is operated in the periodic flow mode with the dry ice the data collected had a peculiar distribution within the bins. The first bin always contained one data point, the next bins were generally empty and the remaining data were contained in the later bins comprising the cycle. The data obtained in the bins near the end of the cycle had no repeatable structure and no explanation for only obtaining velocity data near the end of the cycle has been proposed. When the LDA system is operated in other flow fields with higher velocities and data rates, realistic results are obtained.

As discussed in more detail in the next section, the thin fog layer is the only region where significant numbers of particles occur. The LDA measurements must be made in this thin region since the LDA system measures the velocity of particles that are assumed to be moving with the flow. In this thin region the particles must leave the dry ice surface at a velocity different from the gas flow, adjust to the gas flow velocity and then come to rest at an equilibrium height of three to five millimeters. Clearly it would be difficult to locate the region where the particles will be moving with the gas flow. In an attempt to circumvent the difficulties associated with the low velocities normal to the dry ice, measurement of the oscillating flow velocities parallel to the dry ice was attempted. In this direction the velocities are large, up to tens of meters per second at chamber resonance. Again the measurements must be made in the fog layer to obtain sufficient particle density. This location limits the measurements to the acoustic boundary layer, the convected Stokes layer, and may be confused by the complicated flow structure and particle dynamics occurring there.

Particle Dynamics. The difficulties experienced with the use of the LDA system has motivated an analytical investigation of the dynamics of particles generated at the dry ice surface and moving through the flow field. The model is a rather simplified one but it yields some insight into the difficulty of LDA measurements in this flow field. The dynamics of a small particle in the vertical direction, away from the dry ice, and in the horizontal direction, parallel to the dry ice, are separable. Only the vertical motion is discussed here.

Water particles, locally embedded in the commercial dry ice during its manufacturing, are believed to be ejected from the subliming surface when it absorbs thermal energy. The total amount of water included in the dry ice is less than one percent by weight. These particles collect above the surface at a height of about 3 to 5 mm and form a static, uniform and flat fog layer, Figure 33. This fog layer is an assembly of tiny particles of liquid water and/or water ice numbering several hundred per cubic centimeters and having radii of about 5 μm . The formation of the layer is due to the balance of viscous drag, introduced by the gas flow generated by the subliming dry ice, and gravity on the particles. The layer has a thickness of about 2 mm because of the distribution of the particle sizes. Large particles with high ejection velocity may pass through the layer and then fall back into it, an effect called overshooting, Figure 34. The velocity of smaller particles may match the gas flow velocity before the particle



Figure 33
Photograph of the steady fog layer



Figure 34
Photograph of the fog layer with overshooting

approaches the layer and becomes stationary in the vertical direction. This region of particle motion at the flow velocity is necessary if LDV measurement can be successfully completed. The motion of all size particles is highly damped so that the particles do not oscillate about their static-equilibrium positions.

Research on particle motion where the particles are free to move through a fluid under the action of some body force such as gravity have been carried out for certain conditions and applications [32-35]. To the best of the authors knowledge, particles moving in a viscous flow field in which there is a velocity gradient as well as gravity, have not been studied analytically. The following results are useful for evaluating techniques, e.g., flow visualization or laser Doppler velocimetry, in which suspended particles must closely follow the fluid motion.

After ejection from the subliming surface, the motion of a particle is governed by gravity and viscous drag. Viscous drag, due to the particle's relative velocity with respect to the gas flow, produces a downward force. Due to the small Reynolds number, Stokes flow has been employed to calculate the drag force. The water particles are assumed to be spherical, rigid and of constant radius. Under these assumptions the drag force exerted on a moving sphere of radius r by a viscous fluid is given by

$$F_d = \frac{1}{2} \rho u^2 \pi r^2 C_d \quad (16)$$

here ρ is the density of the gas, u is the velocity of the particle relative to the gas, and C_d the drag coefficient of the particle. In terms of the Reynolds number, Re , (16) can be written in the form

$$F_d = \frac{\pi}{4} \mu r u Re C_d \quad (17)$$

where μ is the dynamic viscosity of the gas. For very small Reynolds numbers, Stokes flow around a sphere gives $C_d = 24/Re$. It is found experimentally that this result is valid for Reynolds numbers less than unity. In the dry ice simulation, $Re = 0.02$ for $u = 1$ cm/s and $r = 5 \mu\text{m}$.

The difference between the weight and buoyancy force on the sphere is given by

$$F_g = \frac{4}{3} \pi r^3 g (\rho_p - \rho) \quad (18)$$

here ρ_p is the density of the particle. Using Newton's second law, the governing equation for motion of a particle can be written as

$$\frac{4}{3} \pi r^3 \rho_p \frac{d^2 y_p}{dt^2} = F_d - F_g \quad (19)$$

In this equation y_p is the distance the particle is located above the dry ice surface. We assume the flow velocity component in the vertical direction is given by

$$u(y) = U_o - \frac{\partial U}{\partial y} y \quad (20)$$

It should be noted that this linear velocity profile is a fairly rough approximation of the flow inside the chamber, based on some numerical modelling. The particles, however, only move a very short distance from the surface to their final position in the fog layer and this linear approximation is reasonable over that distance.

The equation of motion of a particle, with the linear velocity profile and where $u = U(y_p) - dy_p/dt$, may be written as

$$\frac{4}{3} \pi r^3 \rho_p \frac{d^2 y_p}{dt^2} = 6 \pi \mu r \left[\left(U_o - \frac{\partial U}{\partial y} y_p \right) - \frac{dy_p}{dt} \right] - \frac{4}{3} \pi r^3 g (\rho_p - \rho) \quad (21)$$

or

$$\frac{d^2 x}{dt^2} + \frac{2\xi}{\tau} \frac{dx}{dt} + \frac{1}{\tau^2} x = 0 \quad (22)$$

where

$$\tau = \sqrt{\frac{2 r^2 \rho_p}{9 \mu} \left(\frac{\partial U}{\partial y} \right)^{-1}} \quad (23)$$

$$\xi = \frac{3}{2} \sqrt{\frac{\mu}{2 r^2 \rho_p} \left(\frac{\partial U}{\partial y} \right)^{-1}} \quad (24)$$

$$x = y_p - \delta_{st} \quad (25)$$

and

$$\delta_{st} = U_0 \left(\frac{\partial U}{\partial y} \right)^{-1} - \frac{g(\rho_p - \rho) \tau^2}{\rho_p} \quad (26)$$

here the static displacement, δ_{st} , was found from (21) by setting $d^2y_p / dt^2 = dy_p / dt = 0$, and is the position where the particle reaches its static equilibrium, with a balance between the drag force and its weight. From the measured position of the fog layer, it is not difficult to find that the gas flow velocity gradient, $\partial U / \partial y$, at the fog layer is about 2.0 s^{-1} . The position of the fog layer will be discussed further below. For a given flow field, a critical particle radius r_c ($=7.9\mu$ for $U_0=1 \text{ cm/s}$, $\partial U / \partial y=2.0 \text{ s}^{-1}$) can be found by setting $\delta_{st} = 0$ in (26). This critical radius corresponds to the radius of a particle which has a static equilibrium position on the subliming surface, and thus gives an upper bound on the radii of the particles that make up the fog layer.

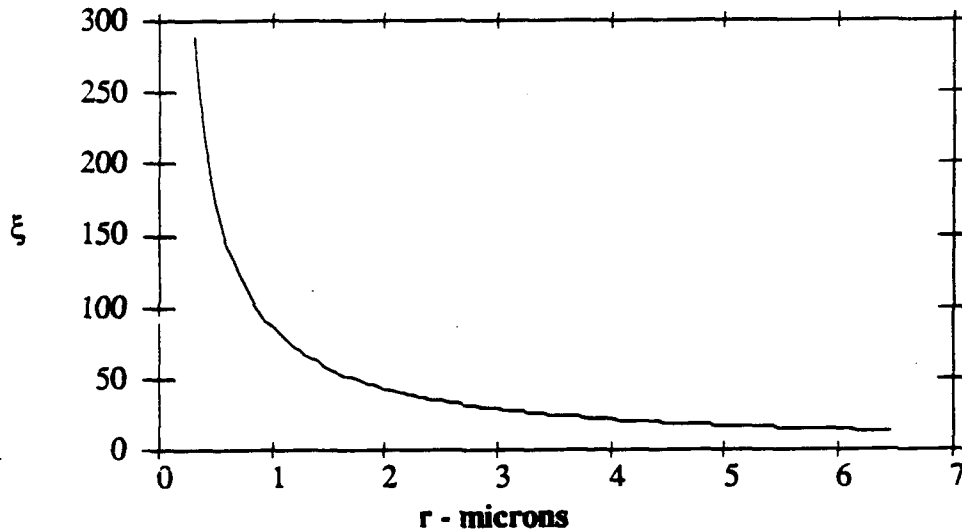


Figure 35
Damping factor versus particle radius

Equation (22) is a damped oscillator equation. The damping factor ξ , a nondimensional parameter, is a function of μ , ρ , ρ_s , and $\partial U / \partial y$. For a given flow field, as the radius of the particle decreases, the damping factor will increase (Figure 35). For the range of interest in the experiments, the damping factor is always greater than one and the motion is overdamped. This is easily seen since at $r_c=7.9\text{mm}$, $\xi=11.023$. and r_c is the radius of the largest particle that can be in the fog layer.

The motion of particles with radii smaller than the critical radius can be found by solving (22). Using the initial conditions

$$y_p(0) = 0 \quad (27)$$

$$\frac{dy_p(0)}{dt} = V_o \quad (28)$$

or

$$x(0) = -\delta_{st} \quad (29)$$

$$\frac{dx(0)}{dt} = V_o \quad (30)$$

where V_o is the velocity of the particle as it leaves the surface. The solution to (22) is, for $\xi > 1$

$$x = A \exp \left[\frac{-\xi + \sqrt{\xi^2 - 1}}{\tau} t \right] + B \exp \left[\frac{-\xi - \sqrt{\xi^2 - 1}}{\tau} t \right] \quad (31)$$

where

$$A = \left[\frac{(\xi + \sqrt{\xi^2 - 1}) \delta_{st} - V_o \tau}{2\sqrt{\xi^2 - 1}} \right] \quad (32)$$

and

$$B = \left[\frac{(\xi - \sqrt{\xi^2 - 1}) \delta_{st} - V_o \tau}{2\sqrt{\xi^2 - 1}} \right] \quad (33)$$

The motion of a particle can be described approximately by the first term in the solution, (31), after a short period of time. This results from the second term decaying much faster with time than the first term for a large value of ξ . With this approximation

$$x = A \exp \left[\frac{-\xi + \sqrt{\xi^2 - 1}}{\tau} t \right] \quad (34)$$

similarly the particle velocity is given by

$$\frac{dx}{dt} = A \left[\frac{-\xi + \sqrt{\xi^2 - 1}}{\tau} \right] \exp \left[\frac{-\xi + \sqrt{\xi^2 - 1}}{\tau} t \right] \quad (35)$$

combining (34) and (35), we get

$$\frac{dx}{dt} = \frac{-\xi + \sqrt{\xi^2 - 1}}{\tau} x \quad (36)$$

or

$$y_p = \delta_s + A \exp \left[\frac{-\xi + \sqrt{\xi^2 - 1}}{\tau} t \right] \quad (37)$$

$$\frac{dy_p}{dt} = \frac{\xi - \sqrt{\xi^2 - 1}}{\tau} (\delta_s - y_p) \quad (38)$$

From (38) it can be seen that the approximate velocity profile of a particle is a linear relation with the height y_p , which has the same form as the gas flow velocity profile.

Using the Taylor expansion for $\sqrt{(\xi^2 - 1)}$ in (38) gives

$$\frac{dy_p}{dt} = U_0 - \frac{\partial U}{\partial y} y_p + O(r^2) \quad (40)$$

For small particles ($r \ll r_c$)

$$\frac{dy_p}{dt} = U(y) \quad (41)$$

When the particles are very small ($r \ll r_c$) their velocity will match the gas velocity after a short transition region, but this still does not answer the question of how well a typical particle will reflect the gas velocity. Displacement versus time and velocity versus time curves for particles of different sizes are shown in Figure 36 and Figure 37. As expected, small particles follow the gas flow closer than large particles. To understand measurements made with the LDV system, it is necessary to know the relative velocity difference β , where $\beta = |U(y) - dy/dt| / U(y)$. Figure 38 shows this relative velocity difference between the gas flow velocity and particle velocities for different sizes and $U_0 = V_0 = 1 \text{ cm/s}$. Particles in the fog layer have a zero velocity in the vertical direction, vertical velocity can only be measured between the subliming surface and the fog layer. As can be seen, the smaller the size of the particle that can

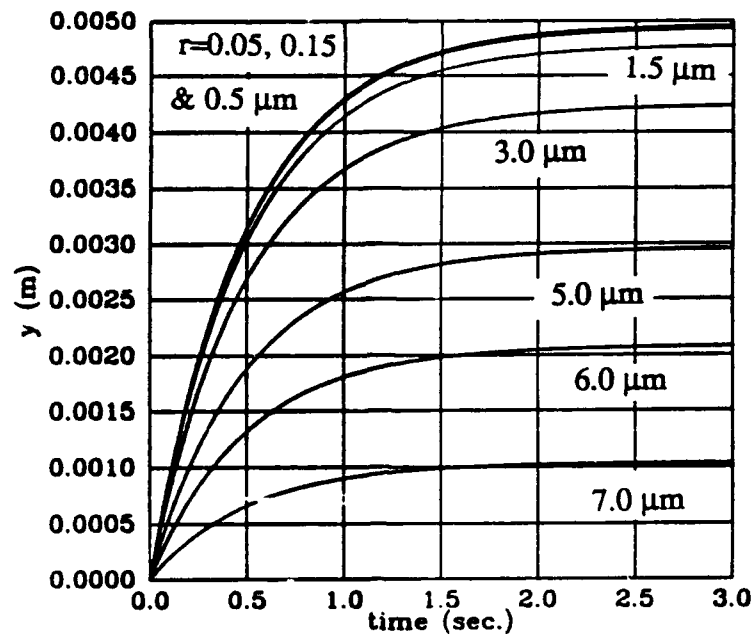


Figure 36
Particle position versus time for several particle radii

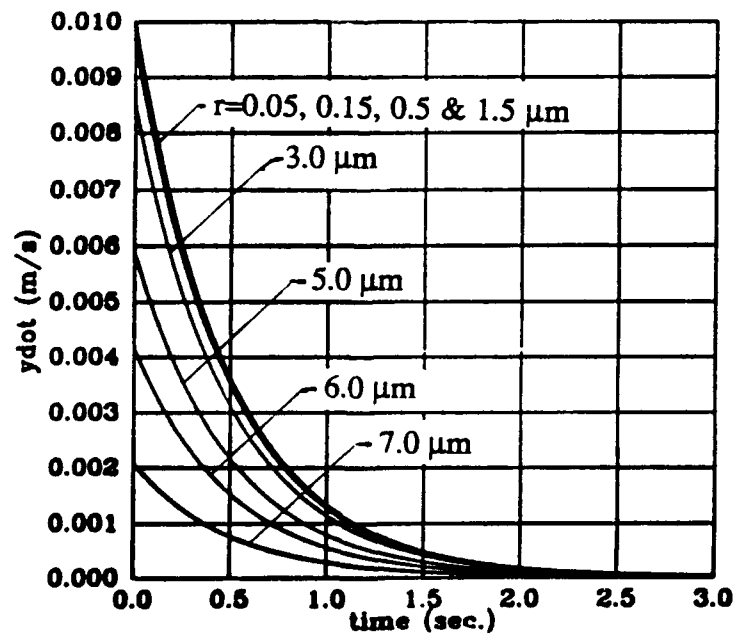


Figure 37
Particle velocity versus time for several particle radii

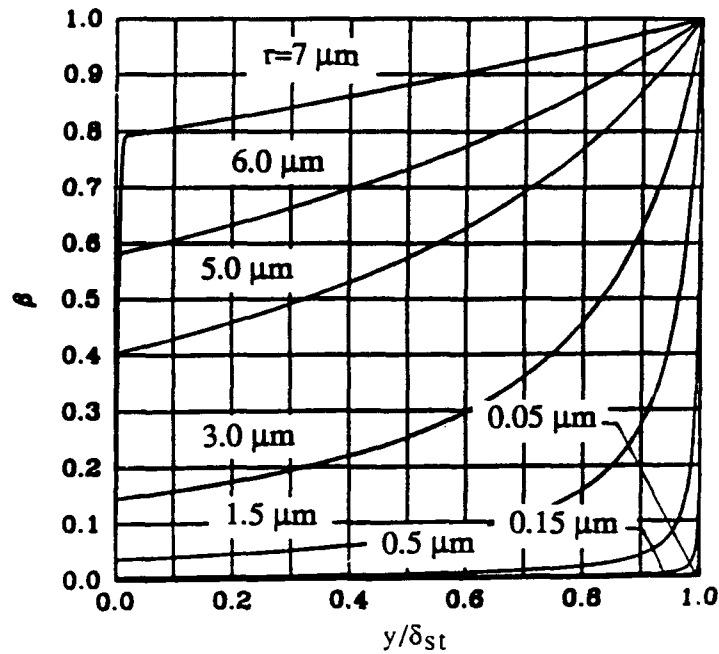


Figure 38
Relative error between the particle velocity and flow velocity as a function of height about the surface for several particle radii

used for the velocity measurement, the more accurate the measurement.. A rapid change in velocity is observed near the surface from these figures. This "jump" is the result of the dominance of gravity in this region. The most meaningful point to measure particle velocity is, clearly, after the particle passes this region of high velocity gradient. After this region the particle velocity has only a small velocity difference from the gas flow for the majority of the motion of the particle. For a particle of $r=3 \mu\text{m}$, the error is within 20%. during most of its motion. Larger particles have a larger error.

Static-equilibrium position for a given flow field and particles with different sizes have different static equilibrium positions (Figure 39). Small particles are suspended higher from the subliming surface staying at the upper part of the fog layer, and larger particles are closer to the surface. The static-equilibrium position is independent of the initial velocity of the particle. It reflects the contribution of the properties of the particle and the gas flow field. All of the particles with radii smaller than r_c have their static equilibrium positions above the subliming surface. Ignoring overshooting, particles will only have a motion in the vertical direction below the fog layer, which is a few millimeters above the subliming surface. This very small region in which LDV measurements can be made makes the measurements difficult. In addition, if the laser beam is close to the dry ice surface, it may stimulate local high sublimation rate which may produce misleading results.

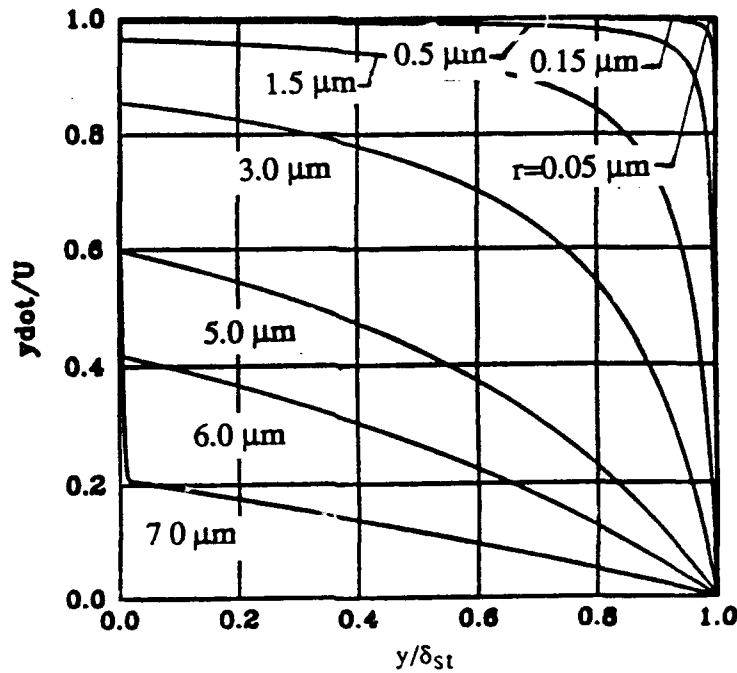


Figure 39
Particle velocity as a fraction of local flow velocity as a function of the fraction of the equilibrium height for several particle radii

When $\xi > 1$, a particle with a high initial velocity may overshoot the fog layer. This large initial velocity appears to be caused by the high sublimation rate at a collection of water particles in the dry ice. This is due to a higher absorption of infrared radiation by water than by dry ice. The extra thermal energy, conducted to the dry ice surrounding the water particles, results in a locally increased sublimation rate. This locally high injection velocity carries the water particles away from the dry ice surface at a high initial velocity. In general, most particles do not overshoot and obtain their equilibrium position from below, but some do. These overshooting particles form a local jet which carries the water particles with it into the chamber. Interestingly, similar phenomena have been reported in the burning of real solid propellant, where nonuniform burning of the propellant can be found [36].

Since $dx/dt = 0$ ($0 < t < \infty$) at the overshooting peak, it is not difficult to find the overshooting region as shown in Figure 40 where $\psi = (\tau V_0 / \delta_{st})$ is the nondimensional initial particle velocity. The curve between the overshooting region and the no overshooting region is given by

$$\Psi = \frac{\tau V_0}{\delta_{st}} = \xi + \sqrt{\xi^2 - 1} \quad (42)$$

or

$$V_o = \frac{\delta_{st}}{\tau} \left[\xi + \sqrt{\xi^2 - 1} \right] \quad (43)$$

Figure 40 shows that with an increase in the particle radius the initial particle velocity needed for overshooting will decrease for a given flow field. This means that a large particle will overshoot easier than a small particle.

This one dimensional analytical investigation of the fog layer allows many important physical explanations about the characteristics of the fog layer to be derived in spite of its simplified character. The analytical model shows that particle ejected from the subliming surface will arrive at a static equilibrium position asymptotically, but after a few seconds the particle will closely approach the final fog layer position. Particles with high initial velocity overshoot their static equilibrium positions. Very small particles match the flow very well when they are below the fog layer, but small particles are hard to measure with the LDV. Measurements of the vertical velocity component laser beam may induce a high local sublimation rates. The best point to

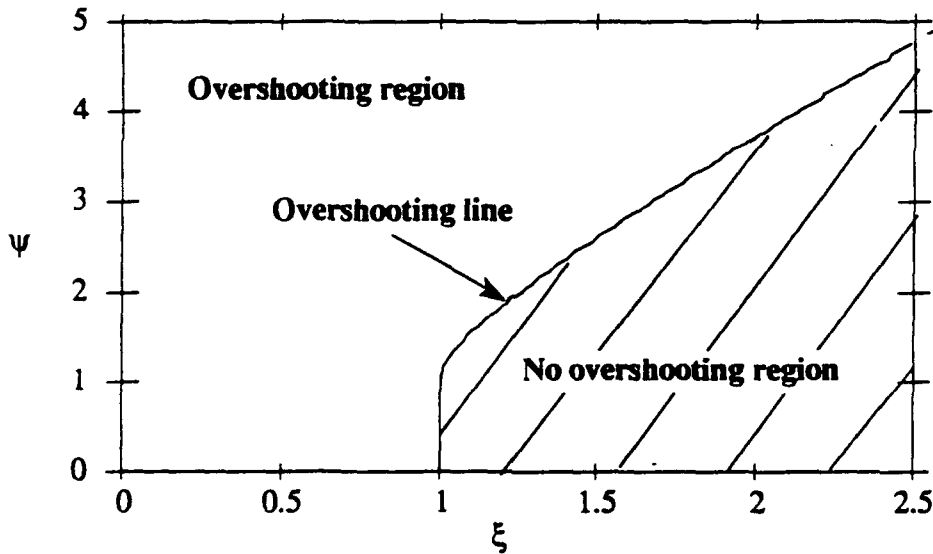


Figure 40
Nondimensional initial velocities and damping ratios when overshooting occurs

measure particle velocity, in the vertical direction, is after particle passes the region of high velocity gradient, since at that point particle velocity is changing rather slowly and has a small velocity difference from the gas flow velocity for the majority of the lifetime of the particle motion.

CONCLUSIONS

Solid carbon dioxide, dry ice, was used to simulate a propellant in an investigation of the fluid dynamic aspects of the flow above a burning propellant. This approach appears to be very successful in providing a relatively simple and realistic method of simulation. The major weakness of the method is the low injection rate that has been obtained. The low injection rate results from the mismatch between the wavelength of the peak of the radiation output from the infrared source and the wavelength of the absorption bands of the dry ice. Attempts were made to modify the absorption of the dry ice by adding water ice and carbon black. These appeared to be successful in small scale experiments but had little effect in the actual experiment. Another method to increase the flow rate would be to use a different source so the peak output would correspond to an absorption band of dry ice. No commercial source with such a peak wavelength has been found. A third approach would be to produce extremely hot carbon dioxide gas which would radiate at exactly the absorption bands of the dry ice. This method has not been investigated and it is not clear if this could be done without dissociating the carbon dioxide. Also it is not known what size device would be needed to produce an adequate amount of radiation.

Flow visualization, hot film anemometry, and mean flow rate correlations all indicate a transition to turbulence of the flow over the simulated burning propellant with an increasing acoustic disturbance. The acoustic Reynolds number for this transition is consistent and independent of the method used to determine it. The transition Reynolds number, however, appears to be dependent on the location of the dry ice. When the dry ice is located near a velocity node, the transition occurs at a much lower acoustic Reynolds number than when the dry ice is near a velocity antinode. Data taken with the dry ice near a velocity antinode is in much closer agreement with the numerical results of Beddini and Roberts [12-14] and the results of other investigators [16-24], with no wall injection, than that obtained with the dry ice near a velocity node. It is possible that this is due to the convection of turbulence from the velocity antinode to the velocity node by the strong acoustic streaming effects that have been observed in the experiment. If transition is locally determined, it would occur first near the center of the tube in which the experiment is conducted, as the amplitude of the acoustic wave is increased. This is due to the higher acoustic velocities occurring at the center of the tube compared to near the ends. It should be possible, if the transition is locally determined, for the center of the tube to be turbulent and the ends laminar. The effect of streaming, however, could convect the turbulence from the center of the tube to the ends giving the appearance that transition occurs at a much lower local acoustic Reynolds number at the ends of the tube than at the center. This is exactly what is observed. If the transition at the end of the tube is expressed in terms of the local acoustic Reynolds number at the tube center, it is found that the transition, at the head end, occurs for a higher Reynolds number than at the center. This lends support to the convection of turbulence explanation.

It appears that a velocity coupling-like phenomenon may be adding energy to the acoustic oscillations in the experiment. This conclusion is based on the higher acoustic amplitudes that are observed with the dry ice located near the tube center and the infrared lamp operating (producing as high injection rate as possible in the

experiment) as compared to the case when the dry ice is replaced by an aluminum plate and there is no side wall injection. These effects are small but are repeatable. The actual amplitudes achieved are sensitive to all energy gains and losses in the experiment and should be investigated further.

The flow never appears to be fully turbulent over a cycle in any condition studied. This characteristic appears to be very crucial in predicting the influence of turbulence in combustion instability and needs to be studied further. It is clear that the occurrence of turbulence plays a very important role in the response of a propellant to velocity oscillations.

The influence of turbulence on the heat transfer rate has been shown to depend on the ratio of excessive acoustic Reynolds number to 0.8 power. This same type of behavior with a Reynolds number to the 0.8 power dependence occurs in steady turbulent flow. Of particular interest is the result that this same correlation appears to apply to the burning rate of actual burning rocket propellant in the presence of oscillations. Since the burning rate of a propellant is strongly determined by the heat transfer to its surface this effect should be expected. Turbulent heat transfer in an oscillating flow does not appear to have been studied, and the 0.8 power dependence appears to have not been observed previously.

Laser Doppler anemometry, although holding much promise, has not proven to be successful in this experiment. Several possible explanations may be given. First, the low velocities achieved, about 1 cm/sec, for the flow from the surface of the dry ice are very near the limit of the capabilities of the system. Second, the dynamics of the particles given off by the dry ice limit the region where the LDA may be used to within a few millimeters of the dry ice surface. Third, there may be a problem in the software of the LDA system.

Clearly this project has raised many questions for future work. Foremost among these is the need for a more detailed investigation of the turbulent heat transfer in an oscillating flow. A brief literature search has failed to locate any information on this subject. Yet understanding oscillating, turbulent heat transfer appears to be the key to understanding velocity coupling. Other questions that have arose also center about turbulent oscillating flow. When does the transition occur at higher injection rates? What are the structural characteristics of a turbulent, oscillating boundary layer? For example, what is the phase relationship between the oscillations at the surface and the oscillations in the "plane wave" region of the flow, near the tube center line? In previous work by Hino et al. [21-22] the turbulent flow appeared to occur only during a portion of the cycle and the flow relaminarized during the remaining part of the cycle. Does this really occur? Does it occur for a limited range of acoustic Reynolds number? What is the effect of relaminarization on the heat transfer and boundary layer? Also what effect does injection have on all of these effects? The answers to these questions are necessary building blocks to a combustion model that includes acoustically induced turbulence and will likely explain velocity coupling.

REFERENCES

1. Hart, W. R. and McClure, F. T., "Combustion Instability: Acoustic Interaction with a Burning Propellant Surface," J. Chem. Phys., Vol. 30, No. 9, 1959, pp. 1501-1514.
2. Culick, F. E. C., "Stability of Longitudinal Oscillations with Pressure and Velocity Coupling in a Solid Propellant Rocket," Combustion Science and Technology, Vol. 2, No. 4, 1970, pp. 179-201.
3. Culick, F. E. C., "Interactions between the Flow Field, Combustion and Wave Motions in Rocket Motors," Navel Weapons Center, TP 5349, June 1972.
4. Culick, F. E. C., "Stability of Three-Dimensional Motions in a Combustion Chamber," Combustion Science and Technology, Vol. 10, 1975, pp. 109-124.
5. Price, E. W., Department of Aerospace Engineering, Georgia Institute of Technology, personal communication.
6. Crump, J. E., and Price, E. W., "Effect of Acoustic Environment on the Burning Rate of Solid Propellants," AIAA Journal, Vol. 2, No. 7, 1964, pp 1274-1278.
7. Stepp, E. E., "Effect of Pressure and Velocity Coupling on Low-Frequency Instability," AIAA Journal, Vol. 5, No. 5, 1967, pp 945-948.
8. Lengelle, G., "Model Describing the Erosive Combustion and Velocity Response of Composite Propellant," AIAA Journal, Vol. 13, No. 3, 1975, pp 315-322.
9. Micci, Michael, Caveny, Leonard H., Sirignano, William A., "Linear Analysis of Forced Longitudinal Waves in Rocket Motor Chambers," AIAA Journal, Vol. 19, No. 2, 1981, pp 198-204.
10. Brown, R. S., Willoughby, P. G. and Dunlap, R., "Coupling Between Velocity Oscillations and Solid Propellant Combustion," Paper No. AIAA-84-0288, AIAA 22nd Aerospace Sciences Meeting, January, 1984.
11. Medvedev, Yu. I., and Revyagin, L. N., "Unsteady-State Erosion of a Powder," Fizika Goreniya i Vzryva, Vol. 10, No. 3, 1974, pp. 341-345.
12. Beddini, R. A., and Roberts, T. A., "Turbularization of an Acoustic Boundary-Layer on a Transpiring Surface," Paper No. AIAA-86-1448, AIAA/ASME/SAE/ASEE 22nd Joint Propulsion Conference, June, 1986.
13. Beddini, R. A., and Roberts, T. A., "Response of Propellant Combustion to a Turbulent Acoustic Boundary Layer," Paper No. AIAA-88-2942, AIAA/ASME/SAE/ASEE 24th Joint Propulsion Conference, July, 1988.

14. Roberts, T. A., and Beddini, R. A., "A Comparison of Acoustic and Steady-State Erosive Burning in Solid Rocket Motors," Paper No. AIAA-89-2664, AIAA/ASME/SAE/ASEE 25th Joint Propulsion Conference, July, 1989.
15. Schlichting, H., Boundary Layer Theory, McGraw Hill, New York, 1968.
16. Vincent, G.E., "Contribution to the Study of Sediment Transport on a Horizontal Bed due to Wave Action," Proceedings of Conference on Coastal Engineering, University of Florida, Vol. 16, 1957, pp. 326-335.
17. Collins, J.I., "Inception of Turbulence at the Bed Under Periodic Gravity Waves," Journal of Geophysical Research, Vol. 68, 1963, pp. 6007-6014.
18. Sergeev, S.I., "Fluid Oscillations in Pipes at Moderate Reynolds Numbers," Fluid Dynamics, Vol. 1, 1966, pp. 21-22.
19. Li, H., "Beach Erosion Board," U.S. Army Corps of Engineers, Washington, D.C., Tech. Memo. no. 47, 1954.
20. Merkli, P., and Thomann, H., "Transition to Turbulence in Oscillating Pipe Flow," Journal of Fluid Mechanics, Vol. 68, 1975, pp. 567-575.
21. Hino, M., Sawamoto, M., and Takasu, S., "Experiments on Transition to Turbulence in an Oscillatory Pipe Flow," Journal of Fluid Mechanics, Vol. 75, 1976, pp. 193-207.
22. Hino, M., Kashiwayanagi, M., Nakayama, A., and Hara, T., "Experiments on the Turbulence Statistics and the Structure of a Reciprocating Oscillatory Flow," Journal of Fluid Mechanics, Vol. 131, 1983, pp. 193-207.
23. Ohmi, M., Iguchi, M., Kakehashi, K. and Masuda, T., "Transition to Turbulence and Velocity Distribution in an Oscillating Pipe Flow," Bull. JSME, Vol. 25, 1982, pp 365-371.
24. Akhavan-Alizadeh, R., "An Investigation of Transition and Turbulence in Oscillatory Stokes Layers," Ph. D. dissertation, Dept. of Mechanical Engineering, MIT, 1987.
25. Raznjevic, K., Handbook of Thermodynamic Tables and Charts, McGraw Hill, New York, 1976.
26. Warren, Stephen G., "Optical Constants of Carbon Dioxide Ice," Applied Optics, Vol. 25, 1986, pp. 2650-2673.
27. Heusser, Eric, "Heat Transfer in a Simulation of a Burning Rocket Propellant using Dry Ice," M.S. Thesis, Mechanical Engineering Dept., University of Utah, 1989.
28. Zucrow, M. J., and Hoffman, J. D., Gas Dynamics, Wiley, New York, 1976.
29. Hinze, J.O., Turbulence, Second Edition, McGraw-Hill Book Company, 1975.

30. Nyborg, W. L., "Acoustic Streaming," Physical Acoustics, Vol. IIB, W. Mason, ed., Academic Press, 1965.
31. Beyer, R. T., Nonlinear Acoustics, U.S. Department of Defense, Department of the Navy, Naval Sea System Command, Washington, D.C., 1975.
32. Clift, R. Grace, J. R. and Weber, M. E., Bubbles, Drops, and Particles, Academic Press Inc., New York 1978.
33. William, F.A., Combustion Theory, The Benjamin/Cummings Publishing Company, Inc., California 1985.
34. Rogers, R. R. and Yau, M. K., A Short Course in Cloud Physics, Pergamon Press, New York 1989.
35. Faeth, G. M. , "Evaporation and Combustion of Sprays," Progress in Energy Combustion Science, Vol. 9, pp 1-76, 1983.
36. Ma, Y., Heusser, E. J., Shorthill, R.W., and Van Moorhem, W. K., " A Simulation of the Flow Near a Burning Solid Rocket Propellant," Paper No. AIAA-89-0301, AIAA 27th Aerospace Sciences Meeting, January, 1989.